Acta
Technica
Jaurinensis

Vol. 8, No.3, pp. 201-217, 2015
DOI: 10.14513/actatechjaur.v8.n3.377
Available online at acta.sze.hu

Stress Analysis and Weight Reduction of a One-Cylinder Engine Crankshaft

P. Horváth, J. Égert

**Department of Applied Mechanics, Faculty of Mechanical Engineering
Information Technology and Electrical Engineering
Széchenyi István University
9026 Győr 1 Egyetem tér, Hungary
horvpe@sze.hu, egert@sze.hu**

Abstract: The paper deals with the weight reduction and the achievement of a more homogeneous stress distribution of a one-cylinder engine's crankshaft, developed for the Formula Student series. In order to achieve this goal, a series of static FEM analysis were performed on the crankshaft. For the FEM analyses, the critical loading and kinematic boundary conditions of the crankshaft were calculated with two different methods. The loads were determined analytically and were verified by Creo Mechanism software. The calculations were done for different engine speeds and - as a result - the critical engine speed, where the highest loads appear could be determined. An essential weight reduction and a more homogeneous stress distribution were achieved on the crankshaft as the result of FEM analysis.

Keywords: crankshaft, finite element method (FEM), weight reduction, stress distribution

1. Introduction

The paper shows the stress analysis of the crankshaft of a one-cylinder engine, designed by the SZEngine team (the stundent's engine development team of Széchenyi István University) for the Formula Student (FS) race series and gives recommendations for the weight reduction of the crankshaft. The FS race tracks feature many curves, slaloms and short, straight sections. These features must also be taken into consideration in the course of designing and developing the proper engine for the race car. The main objective of the engine design is the creation of an engine with the possible lowest weight and the possible highest performance. In order to be able to reduce the weight of the crankshaft, a series of static FEM analysis were performed on the crankshaft. On the basis of the results gained by the analysis, one could reduce the weight of the crankshaft, make the stress distribution more homogenous, and fix the emerging failures in the construction. For the analysis, it is necessary to exactly know the maximum loads acting on the crankshaft therefore – as the first step – the paper deals with this problem. The second part shows the results of the stress analyses and the weight reduction.

The analyzed crankshaft (Fig. 1.) is a construction made of three parts, consisting of a crankpin and two other parts, which includes a web, a counterweight and a half-shaft. The three parts are assembled by an interference fit. The material of the crankshaft is 42CrMo4 alloy steel, while for balancing the crankshaft, tungsten hard metal rods are used, which are also connected by an interference fit into the bores of the counterweight. The material properties of the crankshaft are summarized in *Table 1.*

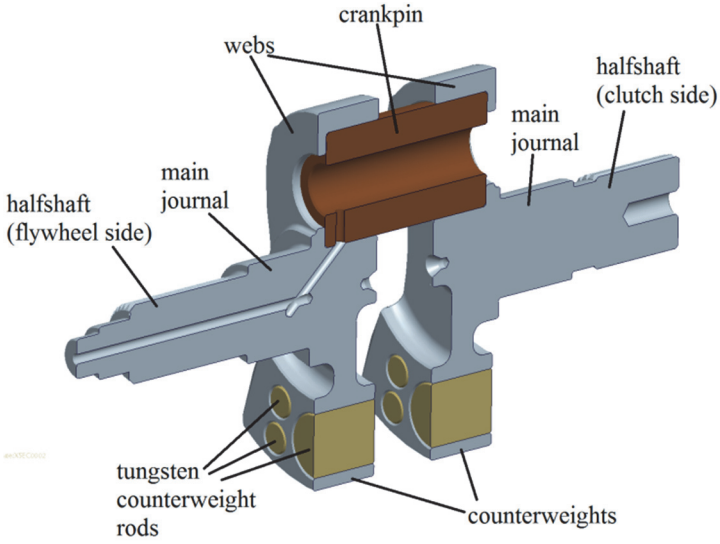

Figure 1. The parts of the analyzed crankshaft

Table 1. Material properties of the crankshaft

Material property	42CrMo4 steel	Tungsten	Unit
Density	7850	19250	kg/m^3
Young's modulus	210000	411000	MPa
Poisson's ratio	0,3	0,28	-
Yield stress	750	1510	MPa
Coefficient of thermal expansion	$1{,}2 \cdot 10^{-5}$	$4{,}3 \cdot 10^{-6}$	1/°C

2. Critical working loads of the crankshaft

The first task is to determine the loads acting on the crankshaft [1], [12], to specify each kind of loading in function of the crank angle and the engine speed. From the loading function the critical maximum loads have to be determined – at which the FEM analysis must be performed.

2.1 Assortment of the working loads

The loads acting on the crankshaft can basically be divided into two groups: loads, which are function of the crank angle and the engine speed, as well as constant loads which are not depending on the revolution. Loads, which are function of the crank angle and the engine speed, originate from three effects:

1) Surface loading acting on the crankpin. These loads originate from the gas pressure inside the engine's cylinder and from the forces of inertia occurring due to the acceleration of the connecting rod and the piston.
2) Body forces resulting from the revolution of the crankshaft.
3) Torque of the flywheel acting on the crankshaft, which occurs due to the moments of inertia of the flywheel and the speed-irregularity (angular acceleration) of the crankshaft.

The constant loads are coming from two effects:

1) Loads from the interference fits (overlap joints).
2) Loads coming from the thermal effects in the engine.

2.2 The surface loads acting on the crankpin

The surface loading acting on the crankpin can basically be determined by two methods: either by using a kind of commercial software dealing with dynamic analysis (for example ADAMS or Creo Mechanism) or by analytically using the principle of impulse and the principle of angular momentum [2]. We determined these loads analytically, but the module of the Creo Mechanism [10], [11] was also used for the verification of the analytically calculated loading.

The gas pressure characteristics were determined by the SZEngine team and it was available in the operating range of the engine (4000-12000 rpm) in 500 rpm angular velocity steps.

During analytical calculations, the angular velocity of the crankshaft was presumed constant, which largely simplifies the calculations, while the failure rate remains at a small value, below 1 % according to [5]. In the course of calculations, at first the kinematic and then the dynamic feature of the connecting rod were determined. After this, the force acting on the crankpin will be derived already from the Newton's law of action and reaction. The kinematic characteristics of the connecting rod were determined on the basis of [3] except for (8) and (11).

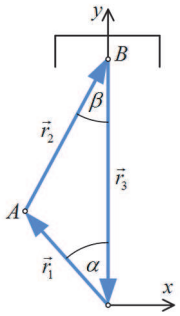

Figure 2. Vector-model of the crank mechanism

In Fig. 2. the vector $\vec{r}_2$ represents the connecting rod and $\vec{r}_1$ models the crank. On the basis of Fig. 2., the following vector-equation can be written:

$$\vec{r}_1 + \vec{r}_2 + \vec{r}_3 = \vec{0}\,. \tag{1}$$

Differentiating once the above vector-equation with respect to time, we get the angular velocity of the connecting rod, while differentiating it twice, the angular acceleration of the connecting rod can be achieved.

$$\omega_2 = \frac{-\omega_1 r_1 \cos\alpha}{r_2 \cos\beta}, \tag{2}$$

$$\varepsilon_2 = \frac{\omega_1^2 r_1 \sin\alpha + \omega_2^2 r_2 \sin\beta}{r_2 \cos\beta}\,. \tag{3}$$

The acceleration of point A is known therefore the acceleration of the arbitrary point P of the connecting rod can be determined by using the angular velocity and the angular acceleration:

$$\vec{a}_P = \vec{a}_A + \vec{\varepsilon}_2 \times \vec{r}_{AP} - \omega_2^2 \vec{r}_{AP}\,, \tag{4}$$

From the evaluation of each term (4), the acceleration of an arbitrary point P is:

$$\begin{aligned}\vec{a}_P = {} & (r_1\omega_1^2 \sin\alpha - \varepsilon_2 r_{AP} \cos\beta + \omega_2^2 r_{AP} \sin\beta)\vec{e}_x + \\ & + (-r_1\omega_1^2 \cos\alpha - \varepsilon_2 r_{AP} \sin\beta - \omega_2^2 r_{AP} \cos\beta)\vec{e}_y\end{aligned} \tag{5}$$

Knowing the mass properties m_h, J_h of the connecting rod and the mass m_d of the piston and the acceleration of an arbitrary point P specified above, the forces acting on the connecting rod (Fig. 3.) can be determined. In Fig. 3. the notation S means the center of gravity of the connecting rod.

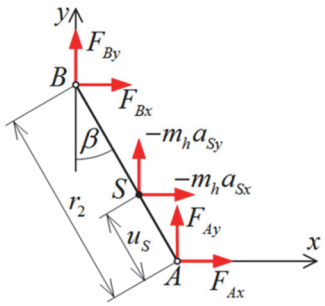

Figure 3. Forces acting on the connecting rod

Applying the principle of impulse for the piston in y direction:

$$m_d a_d = F_g + (-F_{By}) \quad \Rightarrow \quad F_{By} = F_g - m_d a_d\,. \tag{6}$$

Applying the principle of impulse for the connecting rod in y direction:

$$F_{By} + F_{Ay} = m_h a_{Sy} \quad \Rightarrow \quad F_{Ay} = m_h a_{Sy} - F_{By} \,. \tag{7}$$

Applying the principle of angular momentum for the connecting rod rotating about the point *B*:

$$\underline{\underline{J}}_S \vec{\varepsilon}_2 + \vec{\omega}_2 \times \left(\underline{\underline{J}}_S \vec{\omega}_2 \right) + \vec{r}_{BS} \times m_h \vec{a}_S + m_h \left(\vec{\omega}_2 \times \vec{r}_{BS} \right) \times \vec{v}_B = \vec{M}_B \,, \tag{8}$$

where $\vec{v}_B = v_B \vec{e}_y$ is the velocity of point *B,* which value can be determined in the following way:

$$v_B = -\omega_1 r_1 \sin\alpha - \omega_2 r_2 \sin\beta \,. \tag{9}$$

It is important to note that many of the literature sources, such as literature [3] gives only the incomplete form of the principle of angular momentum for a rigid body, which does not contain the fourth term on the left side of the equation (8). According to [6], however, if the principle of angular momentum for a rigid body is applied to a moving point *B* as in the present case – the principle must be completed by the fourth term containing the velocity of the point *B*. In case of leaving this term, the *x* component of the force acting in point *A* shows equation (10), while – taking into consideration this term – it shows equation (11):

$$F_{Ax} = \frac{J_h \varepsilon + m_h a_{Sy} (r_2 - u_S) \sin\beta + m_h a_{Sx} (r_2 - u_S) \cos\beta - F_{Ay} r_2 \cos\beta}{r_2 \sin\beta} \,, \tag{10}$$

$$F_{Ax} = \frac{J_h \varepsilon + m_h a_{Sy} (r_2 - u_S) \sin\beta + m_h a_{Sx} (r_2 - u_S) \cos\beta - F_{Ay} r_2 \cos\beta + m_h \omega_2 r_{BS} \cos\beta v_B}{r_2 \sin\beta} \tag{11}$$

Applying the principle of impulse for the connecting rod in *x* direction:

$$F_{Ax} + F_{Bx} = m_h a_{Sx} \quad \Rightarrow \quad F_{Bx} = m_h a_{Sx} - F_{Ax} \tag{12}$$

Force acting on the crankpin of the crankshaft *C* will be the counter-force of the force acting on point *A* of the connecting rod:

$$F_{Cx} = -F_{Ax} \,, \quad F_{Cy} = -F_{Ay} \,. \tag{13}$$

At 8000 rpm engine speed, the differently calculated tangential and radial components of the force acting on the crankpin, were performed and compared with the results achieved by Creo Mechanism program (Fig. 4. and 5.). In the course of comparison, a proper match could be observed, but – as it can be seen in the figures – a slight deviation could be noticed between the two analytical solutions, which are presented in the tangential force diagram. It is interesting to observe that if the component in *x* direction of force F_A was calculated by applying the incomplete form of the principle of angular momentum (10), an exact match with the result provided by Creo was to be obtained.

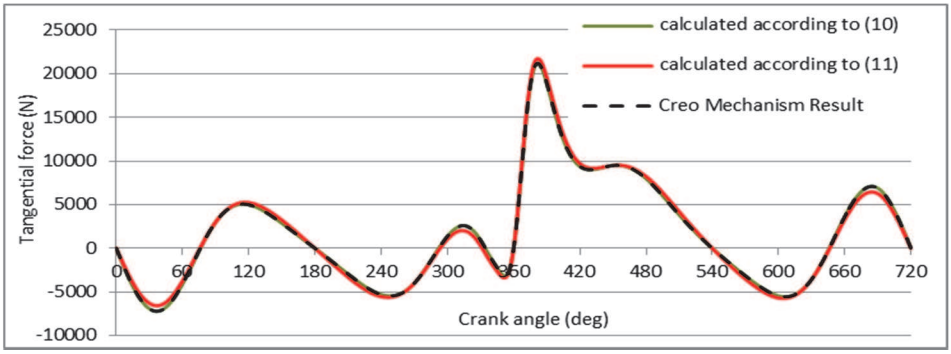

Figure 4. The tangential force acting on the crankpin in function of crank angle at crankshaft speed of 8000 rpm with different calculation methods

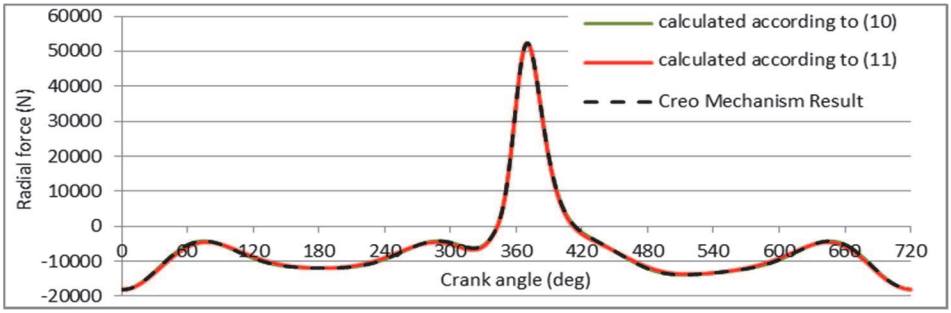

Figure 5. The radial force acting on the crankpin in function of crank angle at crankshaft speed of 8000 rpm with different calculation methods

In reality, the force does not act at a certain point, but on a cylindrical contact surface. The crankpin is assumed to have a sinusoidal pressure distribution. Therefore, the force acting on the crankpin – that was determined above – was transformed into a sinusoidal pressure distribution acting over an angle of $\gamma = 120^{\circ}$ (Fig. 6.).

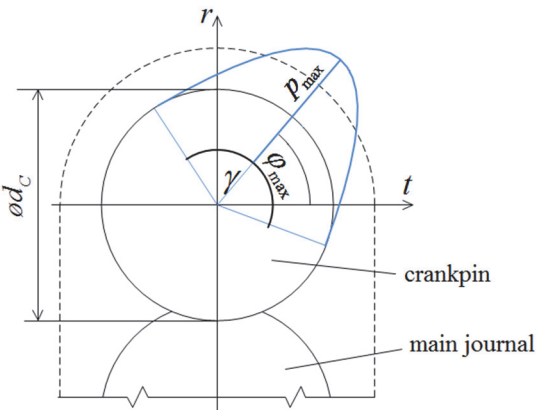

Figure 6. The sinusoidal pressure distribution acting on the crankpin

The pressure curve along the contour of crankpin can be prescribed by the following formula:

$$p(\varphi) = p_{\max} \sin\left[\frac{180}{\gamma}\varphi - \left(\frac{180}{\gamma}\varphi_{\max} - 90\right)\right], \tag{14}$$

where the value $\varphi = 0^{\circ}$ belongs to the *t* axis.

In (14) the pressure constant $p_{\max}$ can be achieved by integrating the pressure surface:

$$F_C = p_{\max} \int_0^{\frac{d_C \pi \gamma}{360}} \int_0^{w_C} \sin\left(\frac{360}{d_C \gamma} s\right) dz\, ds \quad \Rightarrow \quad p_{\max} = \frac{180 F_C}{w_C d_C \gamma}, \tag{15}$$

where w_C is the width and d_C is the diameter of the crankpin.

Since the load acting on the crankpin is the function of the engine speed, with the aid of the equations calculated above, it must be examined in the operational range of the engine (4000 – 12000 rpm) how the loads depend on the change in the engine speeds. At lower engine speeds, the force from gas pressure, while at higher engine speeds, the forces of inertia will be significant. The forces of inertia increase quadratic with the increase of the engine speed. Fig. 7. illustrates the variation of the loads acting on the crankpin at both ends of the operating range.

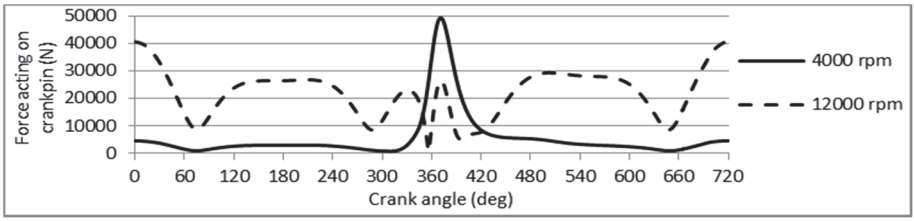

Figure 7. The loads acting on the crankpin in the function of crank-angle at both ends of the operational range

The FEM analysis should be performed at the engine speed, at which the load acting on the crankpin has the maximum value. Fig. 8. shows that the maximum occurs at 6500 rpm engine speed.

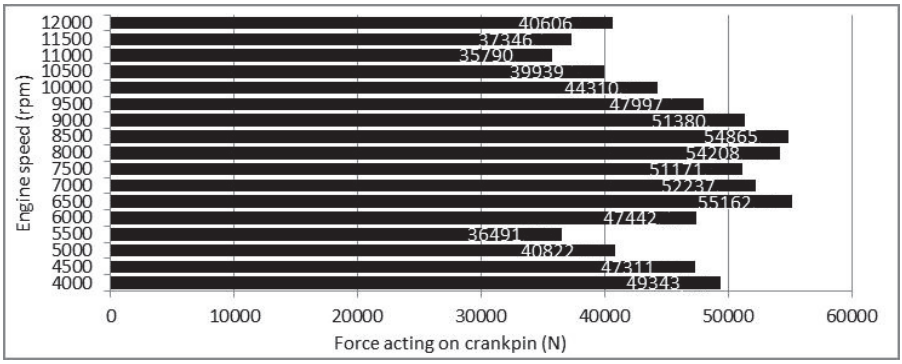

Figure 8. The maximum values of the resultant forces acting on the crankpin in the function of engine speed

2.3. The forces of inertia resulting from the speed irregularity of the crankshaft

This section discusses the instantaneous angular acceleration, which is necessary for the calculation of the body forces resulting from the rotation of the crankshaft, as well as for calculating the torque originating from the flywheel.

The tangential force acting on the crankpin is continuously changing in the function of the crank angle, as it can be seen in Fig. 4. Since the torque of the engine is provided by this force, the torque of the engine will also be irregular, so it will depend on the crank angle.

The inertia of the crankshaft is increased by the flywheel mounted at the end of the crankshaft, which also serves as an energy storing unit. When the instantaneous torque is higher than the medium torque, the crankshaft accelerates, while the flywheel picks up energy. When the instantaneous torque is lower than the medium torque, the crankshaft slows down, while the flywheel delivers energy back to the crankshaft. In the majority of engines, the flywheel – which also includes the clutch – is mounted on one side of the crankshaft. In case of the analyzed single-cylinder engine, the clutch and the flywheel are mounted as two separate parts at both ends of the crankshaft.

In order to be able to determine the speed irregularity, as a first step the medium torque must be calculated. This is a torque value supposed to be constant, which performs the same amount of work as the varying (actual) torque. For this, the torque curve must be integrated for a whole engine cycle and the height of a rectangle of the same width provides the medium value on the basis of the equality of the surfaces.

Fig. 9. illustrates the instantaneous torque and the medium torque at crankshaft speed of 6500 rpm. The work below the medium torque – marked by red stripes – is negative and this decreases the angular velocity, while the work above the medium torque – marked by green stripes – is positive thus increasing the angular velocity.

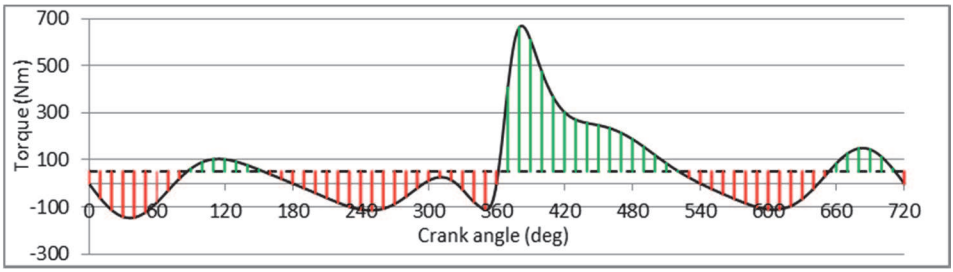

Figure 9. Instantaneous and medium torque acting on the crankshaft at crankshaft speed of 6500 rpm

The instantaneous angular velocity can be obtained from the instantaneous total energy of the system (crankshaft, clutch and flywheel). At first the total energy of the system at $t = 0$ must be determined and then the negative and positive work marked with red and green stripes in Fig. 9. must be added to this average value. So, the total energy of the system at a given time and crank-angle is:

$$E(\alpha_n) = E_0 + \int_0^{\alpha_n} \left[M(\alpha) - M_K \right] d\alpha \,, \tag{16}$$

where E is the energy, resulting from the rotation of the crankshaft, clutch and flywheel and M_K is the medium torque. Knowing the instantaneous total energy of the system, the instantaneous angular velocity of the crankshaft can easily be determined:

$$\omega_1(\alpha) = \sqrt{\frac{2E(\alpha)}{J_f + J_t + J_l}} \,. \tag{17}$$

where J_f, J_t, J_l are the moments of inertia with respect to rotation-axis of the crankshaft, the clutch and the flywheel.

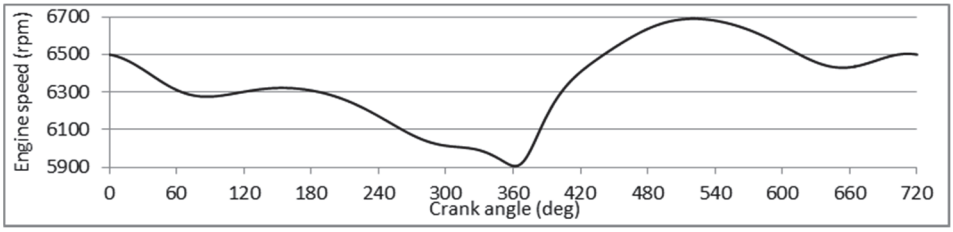

Figure 10. Variation of crankshaft speed at initial crankshaft speed of 6500 rpm

The flywheel – with its high inertia – tends to decrease the irregularity during the work of the engine. This balancing effect causes high torque on the crankshaft. The torque, resulting from the inertia of the flywheel can be calculated by multiplying the inertia of the flywheel with the instantaneous angular acceleration, which is the derivative of the instantaneous angular velocity with respect to time:

$$\vec{M}_t = -J_l \vec{\varepsilon}_l = -J_l \frac{d\vec{\omega}_l}{dt} \,. \tag{18}$$

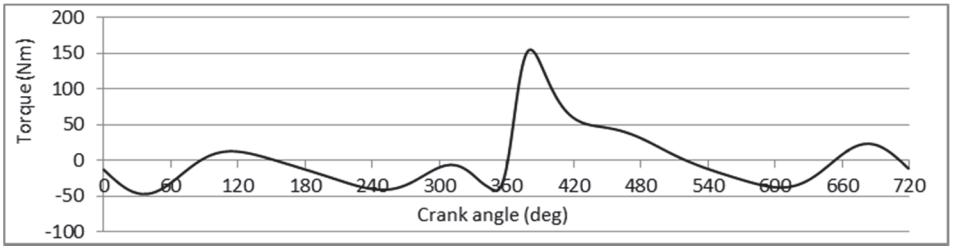

Figure 11. Variation of torque caused by the flywheel at crankshaft speed of 6500 rpm

2.4. Constant loads

In the crankshaft the crankpin is mounted by interference fit and the tungsten rods applied as counterweights are also fit by interference. At these fits / joints – due to the applied interferences – constant loads occur. The interferences were available as constructional parameters. Due to the lack of thermal analysis of the engine, 100 °C

constant, homogenous temperature distribution was supposed as thermal loading on the whole volume of the crankshaft.

3. FEM analysis of the crankshaft

In order to be able to reduce the weight of the crankshaft and to make the stress distribution on it more homogenous, a series of static FEM analysis [7], [8], [9] were conducted on the crankshaft.

3.1. Creating the mechanical and FEM model

The FEM-mesh was created by ANSYS Workbench software [4]. The crankshaft was meshed in quadratic tetrahedron elements. The generally applied element size was 3 mm, while in areas considered to be critical (like the main journal fillet or surfaces connected by interference fit), element sizes of 1 and 2 mm were applied. The total number of elements is 188 152 which contain 306 788 nodes. In the previous chapter it has been stated that the crankshaft receives the highest loading at 6500 rpm engine speed, therefore the finite element analysis was carried out at this nominal engine speed. Fig. 12. shows the meshed crankshaft, while the areas of boundary conditions and applied loads are illustrated in Fig. 13.

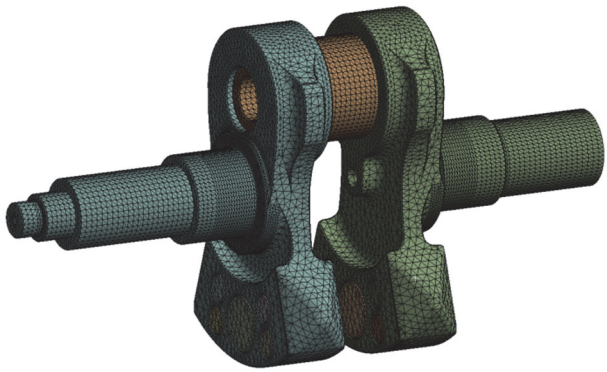

Figure 12. FEM model of the crankshaft

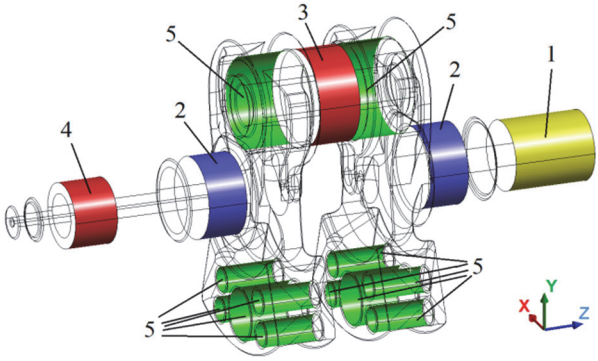

1. Clutch contact surface fixed in rot-z direction
2. Elastic support on the contact surface of the main journals bearings
3. Sinusoidal pressure distribution
4. Torque applied on the contact surface of the flywheel
5. loads resulting from interference

Other loads:

- body forces caused by angular velocity
- 100 °C heat load

Figure 13. The areas of boundary conditions and applied loads

3.2. Evaluation of the finite element analysis

In the course of the finite element analysis, the stress distribution of each special load was examined at first separately thereby the weight of each load could be determined. Then the stress distribution of the total load was also calculated, on the basis of which the possible weight reduction may be performed.

3.2.1. Stress distributions from constant loads

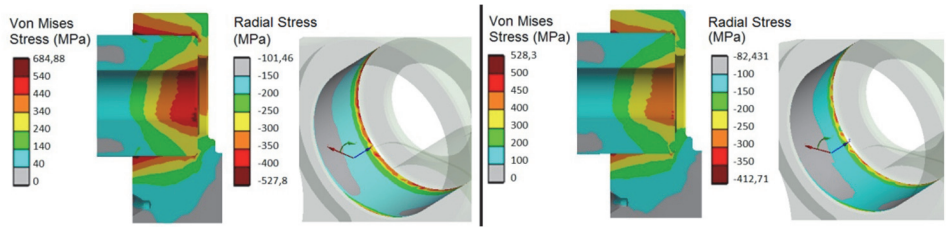

(a) Interference of 0,1 mm *(b) Interference of 0,08 mm*

Figure 14. Von Mises stress distribution and the radial stress distribution on the surface of the bore of the crank-throw

Fig. 14. illustrates the von Mises stress distribution and the radial stress distribution (negative contact pressure distribution) occurring on the surface of the bore of the webs occurring as a result of interference of 0,1 and 0,08 mm, i.e. at both ends of the tolerance range. From this figure, it can be stated that – in both cases – very high von Mises stresses occur furthermore the maximum values of the contact pressure ensuring the joint are also rather high presumably the application of smaller interference would be sufficient. As a result of the 0,01 mm interference of the hard metal rod which serves as counterweight, on the counterweight part, about 300 MPa maximum von Mises stresses occurred.

During the analysis of the thermal load, the above mentioned kinematic boundary conditions were not applied, since – as a result of the thermal effects – the parts ensuring the kinematic boundary conditions would also expand and this could not have been taken into account by the modeling. As a result of the thermal load, not too high stresses occurred. The equivalent von Mises stresses of about 300 MPa occurring at interference fit of the counterweights decreased by half due to the different coefficients of thermal expansion of tungsten and steel (Fig. 15.).

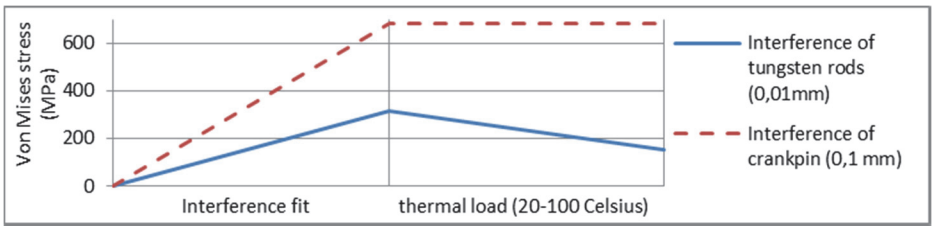

Figure 15. Maximum von Mises stresses occurring as a result of interference fits and the thermal load

3.2.2. Stress distributions from varying loads in function of crank angle

Fig. 16. illustrates the maximum von Mises stresses caused by the varying loads in function of crank angle.

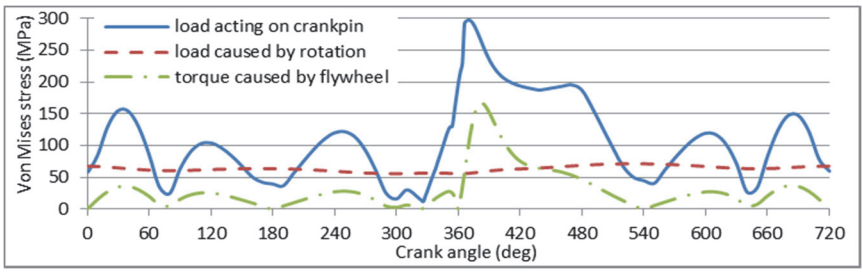

Figure 16. Variation of maximum von Mises stresses caused by the individual loads in function of crank angle

Fig. 17. shows the stress distribution of each load at the crank angle, where the maximum von Mises stress occur. On the basis of the results, the following conclusions could be drawn:

- The maximum equivalent von Mises stress acting on the crankpin occurs at 371^{o} crank angle, this means around the ignition its magnitude is about 300 MPa. The maximum von Mises stresses occur between the fillet of the web and at the main journal (Fig. 17.a).
- The maximum von Mises stress caused by the forces of inertia varies according to the angular velocity. The stresses occurring here are much lower compared to stresses caused by former two loads (max. 70 MPa). The highest stresses are occurring between the main journal and the counterweight (Fig. 17.b).
- The maximum von Mises stress occurring as a result of the torque caused by the flywheel varies according to the variation of the torque. The highest stresses occur on the surface of the half shafts (Fig. 17.c).

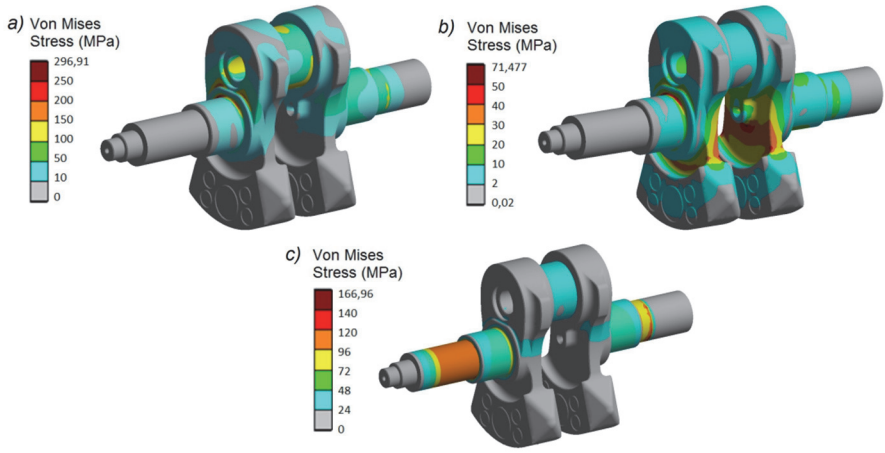

Figure 17. The maximum von Mises stresses occurring from
a) loads on the crankpin b) rotation of the crankshaft c) torque by the flywheel

3.2.3. Checking the effect of the element's size

In order to check the accuracy of the applied finite element-mesh discussed in chapter 3.1, the above described analysis was carried out with two different element size-variations as well, including a denser / finer mesh - the size (number of elements) of which was double of the original mesh - as well as a coarser mesh, the size of which was half of the original mesh.

Fig. 18.*a* illustrates the maximum Von Mises stresses in case of different loads and different element sizes. Fig. 18.b illustrates the minimum radial stresses (maximum contact pressure) on the surface of the web's hole in case of 0,1 mm interference. As it can be seen from the figures, in general, the difference between the original and the finer mesh is smaller than the difference between the original and the coarser mesh, so the values converge by fining the mesh. In case of interference fit, practically there is no difference between the results provided by the original and by the finer mesh. There is no essential difference between the results of the original and those of the finer mesh in other cases, either. Considering this small difference and the significantly higher computation resources demanded by a finer mesh, the further analysis was performed with the original mesh.

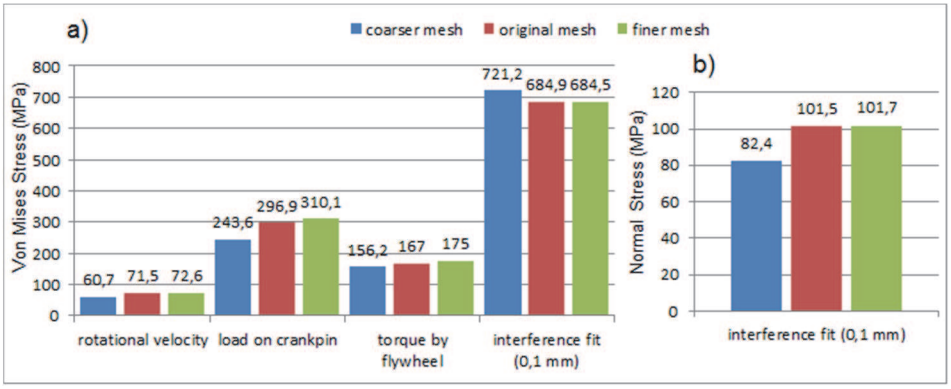

Figure 18. The maximum von Mises and radial stresses in case of different loads and different mesh density

3.2.4. Stress distributions from total load

Fig. 19. demonstrates the stress distributions caused by critical total load.

At the critical total load, the following statements can be made:

- The highest von Mises stresses occurred from the interference fit between the web and the crankpin. This interference loading causes the dominant influence on the stress distribution.

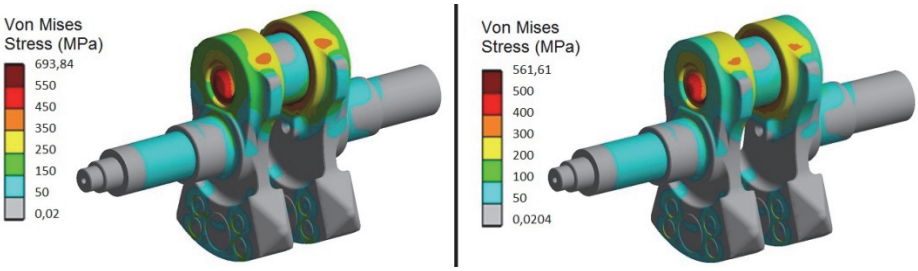

(a) Interference of 0,1 mm *(b) Interference of 0,08 mm*

Figure 19. Equivalent von Mises stress distributions caused by critical total load

- The maximum stress values do not depend on the angle position, so the variation of the stress caused by total load will be approximately constant in function of crank angle.
- The fact that stresses caused by interference are dominating, can be regarded as a constructional failure. Therefore – prior to the weight reduction – this constructional failure should be fixed.

3.2.5. Correction of the constructional failure

On the basis of the aforementioned, stress caused by interference is too high furthermore the contact pressure ensuring the contact is also more than necessary. Therefore this constructional failure had to be eliminated first. In order to be able to determine the minimum necessary contact pressure, it has to be examined how the minimum value of the contact pressure varies on the surface of the bore of the web while applying the total load during a whole engine cycle.

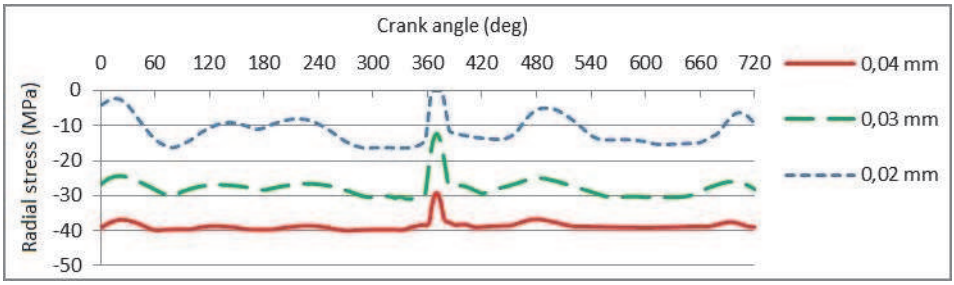

Figure 20. Variation of the minimum radial stress (maximum contact pressure) in function of crank angle in case of different interferences

In case of interference of 0,02 mm, the minimum value of the contact pressure around ignition reaches zero value, so there will be disconnection between the crankpin and the bore, it is to be feared that the crankpin will become loose, therefore at least 0,03 mm interference is necessary in order to be able to properly ensure the interference fit (Fig. 20.). As there is no torsional or axial load between the crankpin and the bore of the web, sliding won't occur between connecting components, so we didn't take it into consideration.

3.3. The modified geometry

On the basis of the results of the finite element analysis, it can be stated that the stress distribution of the crankshaft is not too homogenous. There are areas in which only very small stresses occur, so it is reasonable to remove material from there, while in other areas too high stresses occur, so they must be reduced by proper constructional modifications. The modifications that were carried out can be summarized as follows:

- Increase of the inner bore's diameter of the shafts and pins: higher stresses typically occur on the outer surface of the shafts / pins, while only minimum stresses occur inside them, therefore it is reasonable to remove material from there. In case of the inner bores, the following modifications were carried out:
  - The diameter of the oil bore was increased from 3 mm to 10 mm
  - The diameter of the bore on the clutch side was increased from 8 mm to 16 mm, while its depth was increased from 20 mm to 64,5 mm
  - The inner bore of the crankpin was increased from 15 mm to 20 mm
- The following modifications were carried out in the geometry of the webs:
  - Removal of the "ears" of the webs. Since only small stresses occurred here, they have been removed in order to reduce the weight.
  - Removal of the "shoulder part" of the webs, as a result of which weight reduction was achieved on the one hand, while on the other hand, the stress distribution resulting from the interference fit between the web and the crankpin could be made more homogenous.
  - Reduction of the width and thickness of the web in order to be able to reduce the weight.
  - The rounding / fillet between the main journal and the web was increased from 1,5 mm to 2 mm, by which – as a result of the load acting on the crankpin – the highest stress occurring at the fillet area could be reduced and therefore the stress distribution could be made more homogenous.
- Modification of the counterweight part. Due to the modifications carried out in the previous two steps, the balance of the crankshaft has changed. Due to the increase of the inner bore of the crankpin, as well as due to the removal of material from the upper part of the web, the center of gravity of the crankshaft was shifted into the direction of the counterweights. In order to be able to restore the balance of the crankshaft, the mass of the counterweight had to be reduced. This could be achieved by two kinds of modification:
  - The width and thickness of the counterweight part were reduced.
  - Instead of four small and one large tungsten rods serving as counterweights, five small tungsten rods were installed.

The comparison of the original and modified crankshafts can be seen in Fig. 21.

The extent of the minimum necessary interference was examined by applying the method indicated in chapter 3.2.5. also for case of the modified geometry. In the course of this, it was found that in case of the modified geometry minimum 0,04 mm interference is necessary. Fig. 22. demonstrates the von Mises stress distributions caused by critical total load in the modified construction.

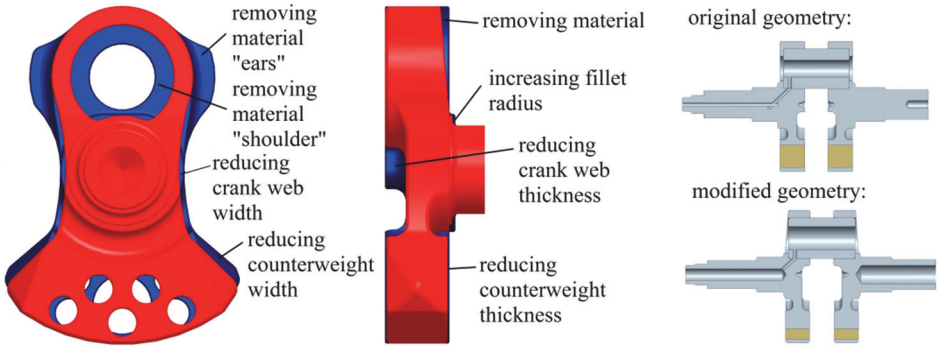

Figure 21. Constructional modifications carried out on the crankshaft

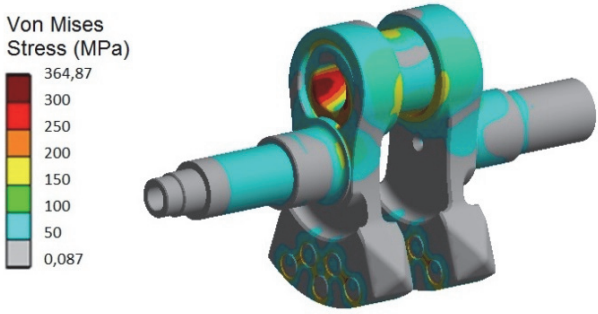

Figure 22: Von Mises stress distribution of the modified crankshaft caused by critical total load

Summary

For the analysis, the critical loads acting on the crankshaft were analytically determined. In the course of this, we have stated that the highest load occurs on the crankshaft at a speed of 6500 rpm, therefore the series of static FEM analysis were performed at this engine speed. The results of the FEM analysis have shown that the crankshaft has a constructional failure, because the equivalent von Mises stress caused by the interference between the crankpin and the web was significantly higher than the stresses caused by the combustion. As a first step, this failure was eliminated by decreasing the extent of the interference. From the FEM analysis it can also be concluded, that there are several areas on the crankshaft, at which very small stresses occur, so material was removed from these areas. As a result of the constructional modifications, the stress distribution became more homogenous furthermore the weight of the crankshaft could be reduced by 19 %.

References

[1] Dezsényi Gy: Design and testing of internal combustion engines (in Hungarian). Nemzeti Tankönyvkiadó, Budapest, 1989.

[2] Montazersadgh FH, Fatemi A: Stress Analysis and Optimization of Crankshafts Subject to Dynamic Loading. International Journal of Materials and Manufacturing, SAE International, Vol. 1, Issue 1, pp. 211-217, April 2009.

[3] Wilson CE, Sadler PJ: Kinematics and Dynamics of Machinery. Harper Collins College Publishers, 1993.

[4] ANSYS 14.5 Mechanical APDL Theory Reference. Ansys Inc., 2012.

[5] Shenoy PS: Dynamic Load Analysis and Optimization of Connecting Rod. Master of Science Degree in Mechanical Engineering, The University of Toledo, 2004.

[6] Király B: Dynamics (in Hungarian). Miskolci Egyetemi Kiadó, Miskolc, 1998.

[7] Zienkiewicz OC, Taylor RL: The Finite Element Method. Fifth edition, Vol. 1. The Basis, Butterworth-Heinemann, 2000.

[8] Zienkiewicz OC, Taylor RL: The Finite Element Method. Fifth edition, Vol. 2, Solid Mechanics, Butterworth-Heinemann, 2000.

[9] Bathe KJ: Finite-Elemente-Methoden. Springer Berlin, 2002.

[10] Toggod R, Zecher J: Creo Parametric 2.0 Tutorial. SDC Publications, 2013.

[11] Chang K-H: Mechanism Design with Creo Elements/Pro 5.0, SDC Publications, 2011.

[12] Pulkrabek WW: Engineering Fundamentals of the Internal Combustion Engine. 2nd Edition, Prentice Hall, 2003.

Acta
Technica
Jaurinensis

Vol. 8, No.3, pp. 218-229, 2015
DOI: 10.14513/actatechjaur.v8.n3.388
Available online at acta.sze.hu

Evaluation of Head Movements in Short-term Measurements and Recordings with Human Subjects using Head-Tracking Sensors

Gy. Wersényi[1], J. Wilson[2]

[1]Széchenyi István University, Department of Telecommunications
Egyetem tér 1, H-9026, Győr, Hungary
E-mail: wersenyi@sze.hu

[2]Georgia Institute of Technology, Interactive Media Technology Center, Atlanta
E-mail: jeff.wilson@imtc.gatech.edu

Abstract: Measurements for spatial hearing research, binaural recordings, virtual reality techniques etc. often rely on Head-Related Transfer Functions of human subjects and head-tracking techniques. Individually measured HRTFs and recordings on human heads may result in more accurate localization and sound field rendering. On the other hand, the measurement and recording procedure raise new problems such as decreased signal-to-noise ratio or subject comfort. For measurements with human subjects lots of methods are used from free heads to different head fixation methods. In this paper, we report an experiment that was conducted using commercially available sensors with the goal of characterizing the range of subject head movements in various postures under various circumstances. The study analyses the range of unwanted head movements during measurements using two sensors, 3-min sessions and four body positions based on the circular angle variance, errors in yaw-pitch-roll directions and magnitude of standard deviation. Results of 16 participants show errors about 2 degrees and magnitudes of standard deviation of 2-8 cm depending on the situation as well as a preference for sitting instead of standing posture.

Keywords: head movement, binaural recording, HRTF, visual tracking

1. Introduction

Measurements with human individuals that require stability of the subject are part of several research areas. These include medical applications, engineering and information technology approaches. The common problem is that subjects have to be instructed to be motionless, because even unwanted small movements of the body can distort data

capture. Therefore, different fixing methods are usually applied from simple head-rests to full-body fixations. Fixing installations, however, can interact with the measurement equipment (reflections, electromagnetic effects etc.), and fixation itself can increase discomfort of the subjects.

1.1. Measurements in spatial hearing research with human subjects

From the sound engineering point of view individual measurements with human subjects are dealing with this problem. Virtual audio simulators, auditory displays use the human Head-Related Transfer Functions (HRTFs) for rendering soundscapes with proper directional information [1, 2, 3, 4]. Sound sources are filtered with the left and right ears' HRTFs respectively. Localization performance is usually decreased in a virtual audio environment due to headphone induced errors (in-the-head localization, front-back reversals etc.) and due to lack of head motion [5, 6, 7, 8, 9]. Furthermore, individually measured HRTFs generally increase localization and overall performance in a virtual audio environment [10-13]. In free-field environments even small head movements of about 1-2 degrees can lead to interaural differences and thus, resolving in-the-localization problems. This can be beneficial in a simulated virtual environment as well [14].

Measurements of individual HRTFs require two-channel recordings within or at the entrance of the blocked earcanals [13]. Subjects are usually seated on a chair in the anechoic chamber with or without head fixation. Multichannel loudspeaker arrays from different spatial directions deliver broadband excitation signals, such as white noise, MLS signals or impulses. In general, the overall signal-to-noise ratio, accuracy, repeatability and spatial resolution are low due to the relatively short measurement time [12]. In contrast to dummy-head measurement techniques, this procedure is quite uncomfortable for the subjects.

1.2. Overview of Literature Survey on Head and Body Motion Effects during Measurements

There is only a few measurement data about the extent of unwanted head and body movement of subjects instructed to be stationary. Lot of these data can be found in the literature of medical sciences.

In case of Functional connectivity MRI (fcMRI) head motion is a confounding factor. Children move more than adults, older adults more than younger adults, and patients more than controls. Head motion varies considerably among individuals within the same population [15]. Mean head displacement, maximum head displacement, the number of micro movements (> 0.1 mm), and head rotation were estimated in 1000 healthy, young adult subjects. Head motion had significant, systematic effects on several network measures and was associated with both decreased and increased metrics.

In functional magnetic resonance imaging (fMRI) head motion can corrupt the signal changes induced by brain activation. For reducing motion-induced effects a full three-dimensional rigid body estimation of head movement was obtained by image-based motion detection to a high level of accuracy [16]. A high level of consistency (rotation < 0.05°) was demonstrated for detected motion parameters.

Another experiment included 40 subjects [17]. Volunteers were examined lying still and performing two separate head movements to assess detection and compensation of in-plane motion during MRI. Head rotation and translation was detected in all subjects. Values less than 1 degree were measured in lying position.

Methods can be developed to correct for motion artifacts in head images obtained by positron emission tomography (PET). The methods are based on six-dimensional motion data of the head that have to be acquired simultaneously during scanning [18, 19]. The data are supposed to represent the rotational and translational deviations of the head as a function of time, with respect to the initial head position. Motion data were acquired with a volunteer in supine position, immobilized by a thermoplastic head holder, to demonstrate the effects of the compensation methods. PET images can be justified and upgraded with post processing algorithms where serious head motion was present.

Similarly to MRI experiments, engineering approaches often include pattern analysis, video capture or accelerometers [20, 21, 22, 23]. A method for tracking of rigid head motion from video using a 3D ellipsoidal model of the head was proposed that is robust to large angular and translational motions of the head [20]. The method has been successfully applied to heads with a variety of shapes, hair styles, and also has the advantage of accurately capturing the 3D motion parameters of the head. This accuracy is shown through comparison with a rendered 3D animation of a model head. Due to its consideration of the entire 3D aspect of the head, the tracking is very stable over a large number of frames. This robustness extends even to sequences with very low frame rates and noisy camera images.

In our case, the focus is on acoustic measurements and virtual audio display technologies where human subjects are essential part of the procedure, most likely at the stage of individual HRTF acquisition.

In Blauert's early study subjects had to localize a 300 ms sinusoidal signal. The localization blur was not influenced by the fact whether the head was fixed or not. The experiments concluded that if the head should be kept stable without fixings, probability of head movements greater than 1° is less than 5%. It was suggested that for signals shorter than 1 s head fixation is not required [24]. Table 1 shows head movements of ten subjects without head fixation (probability and value).

Table 1. Extent and probability of unwanted head movements of ten subjects without head fixing after Blauert [24]. Mean value of the movements was only 0,22 degrees.

0 - 0,2º	0,2 – 0,4º	0,4 – 0,6º	0,6 – 0,8º
53%	34%	9%	4%

The impact of head tracking on localization is well known in the literature [1, 2, 10, 11]. A study of sound localization performance was conducted using headphone-delivered virtual speech stimuli, rendered via HRTF-based auralization, and

blocked ear-canal HRTF measurements [11]. The independent variables were chosen to evaluate commonly held assumptions in the literature regarding improved localization: inclusion of head tracking, individualized HRTFs, and early and diffuse reflections. Significant effects were found for azimuth and elevation error, reversal rates, and externalization.

One of the fundamental limitations on the fidelity of interactive virtual audio display systems is the delay that occurs between the time a listener changes his or her head position and the time the display changes its audio output to reflect the corresponding change in the relative location of the sound source. In an experiment, the impact of difference head-tracker latency values were examined on the localization of broadband sound sources in the horizontal plane [25]. Results suggested that head-tracker latency values of less than 70 ms are adequate to obtain acceptable levels of localization accuracy in virtual audio displays.

Although, there exist measurement data about the effect of head motion in virtual audio simulation and localization tasks, there is no data about the extent of unwanted head motions in case of a measurements where subjects have to be stable.

Our goal with this study was to determine the extent of head movements and instability during different environmental conditions (fixation methods) using different state-of-the-art tracking sensors. Results should support both selection of the appropriate tracking sensor for a given application as well as to determine accuracy range for measurement setups with human subjects mostly for audio engineering applications and spatial hearing research.

2. Measurement setups

The measurement setup included two different, state-of-the-art motion tracker devices:

- Intersense ICube3, a sensor offering a low-profile, rugged aluminum enclosure, sourceless 3-DOF tracking with full 360° range, accuracy of 1° yaw, 0.25° pitch and roll with 180 Hz update rate and 4 ms of latency [26],
- Kinect for Windows and Microsoft Kinect API [27]. The Kinect face tracking API does not define accuracy, but appears to be heavily filtered.

Software was developed that can simultaneously collect data from the Isense ICube3 as well as from the Kinect for Windows (including the Kinect face tracker library). The ICube logging has been modified to also grab the associated raw accelerometer data. This can be thought of as a second sensor and is essentially the same as one might see from the accelerometer in a phone or other device with accelerometer. The Kinect log has both position of the head/face and orientation of the face.

Figure 1. The Intersense and the Kinect sensors.

Participants wear the Icube3 on headphones (just for mounting, no audio) on their head and were also tracked by the Kinect. Informal testing indicated no negative effects of the headphones on the user's head as tracked by the Kinect. The following four conditions were defined:

- sitting unsupported (SiU),
- sitting supported (SiS),
- standing unsupported (StU), and
- standing supported (StS).

When sitting supported, the user has backrest and head against the wall. The user also was asked to place their hands on the armrests. When standing supported, the user leans upright against the wall. We assumed this is a good proxy for a more elaborate setup such as adjustable headrest mounted to a chair or "standing stool".

However, in a real HRTF measurement a wall is not suited due to reflections. Also, we were concerned that the Kinect might not work with the participant so close to the wall, but we found that the Kinect was still able to identify the person.

We found five minutes for each condition to be rather boring and quickly uncomfortable for participants. Therefore, we reduced the trial duration to three minutes. Nevertheless, HRTF measurements even with impulse excitation can last longer [31].

Participants underwent four measurement conditions, mentioned previously, in randomized order and one minute breaks between conditions to relax.

Figure 2. Left photo shows the Kinect mounted on a stand aimed at the chair used for seated positions. The right photo shows headphones with the IntertiaCube3 mounted on top.

3. Results

A total of 22 participants completed the experiment. One participant restarted the session due to a software error. Another participant's data was discarded because one of

the conditions failed to get an estimate of face position using the Kinect and wasn't noticed in time to fix the problem. Five additional participants' data was excluded due to substantial failure of the Intersense tracking in the form of large azimuth drift. Azimuth estimates of the ICube must be corrected to the magnetometer measurements of the Earth's magnetic field and is susceptible to interference. We believe there was some intermittent interference or perhaps some occasional initialization failure in the sensor.

The demographic evaluation included height, gender, age and information about any kind of health issues, balancing problems etc. Of the 16 participants not excluded, 10 were male and 6 female. Reported heights ranged from 1.52 to 1.90 meters, with an average of 1.72 meters and a median of 1.74 meters. No health/balance issues were reported.

Before any statistics were calculated, measures were linearly interpolated to match each sensor's target measurement rate. This was done because measurement recording was sometimes delayed slightly due to various reasons including OS interruption, garbage collection, etc. While measurements were very close to uniformly spaced, they were not quite perfect. In the case of the Kinect, an occasional brief loss of a tracking lock was a source of measurement dropout, which could be much longer than the cases above. Kinect face tracking had 4 dropouts over 2 seconds long over all conditions and participants (durations of 14.5, 8.3, 8.0, and 2.2 seconds). Kinect head tracking had one dropout over 2 seconds long overall all conditions and participants of 7.9 seconds. The IntertiaCube3 had no dropouts over 2 seconds. The IntertiaCube3 has a sample rate of 180 Hz and the Kinect has a sample rate of 30 Hz.

For analysis, a simple means of determining how still the participants were for each posture was necessary. For linear measures (position, and acceleration), variance of position was calculated. For angle measures, circular variance was calculated. Circular variance is commonly used for polar coordinates and it can be adapted to 3DOF. Circular variance is defined as 1 minus the magnitude of the mean of the direction vector of an angle. To adapt for 3DOF we calculate the average of the circular variances of the three angles. The closer to 1.0, the tighter the grouping of pose measurements is. This seemed to be the best way to compare the angle measurements. The mean is not directly relevant for linear or angle measures as it is likely very different for each participant due to variations in body shape, sensor mounting, etc. The variance shows the measurements around that mean that indicate movement. For accelerometer values as well as position, the magnitude of the standard deviation of the measurement vector was used rather than presenting the full vector. The acceleration measurement reflects the effects of gravity. However, this influence is removed automatically in calculating the standard deviation.

Results of magnitude of standard deviation of Intersense acceleration (m/s2) were 0.08351 (SiU); 0.06912 (SiS); 0.10440 (StU); and 0.09051 (StS) also indicating less movement in case of sitting and supported situations, furthermore, SD values less than 0.1 m/s^2 are relatively low.

Table 2. Result of the Intersense. Circular Angle Variance (ICAV, left); Kinect Circular Angle Variance (KCAV, right)

	ICAV	KCAV
StU	0,0013	0,0031
StS	0,0010	0,0030
SiU	0,0004	0,0019
SiS	0,0001	0,0033

Table 3. Result of magnitude of standard deviance of position in meters for Kinect Head (left); and magnitude of standard deviance of position in meters for Kinect Face (right). The Kinect logs position of the head/face and orientation of the face used for automated reference.

	M.Stdv. Head	M.Stdv. Face
StU	0,0837	0,0440
StS	0,0208	0,0131
SiU	0,0411	0,0286
SiS	0,0189	0,0177

4. Discussion

One challenge in this sort of study assessing the suitability of a sensor is that ideally one will want to compare the sensor's measurements to a ground truth. This would likely consist of an additional measurement technique superior to the sensor(s) being evaluated. This superior measurement would serve as the ground truth and allow measuring the error of the test sensors. In the case of this study we did not have that ability. The Intersense does have published sensor measurement specifications and we can see that our measurement data fits within those tolerances. We can however compare the Intersense and Kinect to see if they appear to record similar movement across conditions, as well as also considering the practical issues of using the each sensor (e.g. setup, likelihood of tracking loss, etc.).

Results can be evaluated in comparison of the two systems as well as to compare the four conditions. Within the four conditions, there appears to be a general trend that shows that the supported postures allow the participants to be more still than the unsupported postures of the same type of posture. Furthermore, sitting appears to offer more support than standing. Though this has not been formally statistically tested.

Additionally the Intersense tracker seems to be more accurate than the Kinect, whether using angle estimates or raw accelerometer measures.

The Kinect Face Tracking appears to be the least accurate and does not agree with the other measures about stillness of participants across the different postures and support. We believe that this is probably due to the Kinect Face Tracking briefly losing a lock on the participants face and then reacquiring it with slightly different coordinates. This may be happening more often that our analysis of tracking dropout discussed previously, but

with very short durations such that the event doesn't trigger a tracking lost event in the Kinect API. We would otherwise expect the face tracking to at least be more accurate that Kinect head tracking. Also, the Kinect was experienced to be very sensitive to setup whereas the Intersense could be placed on the participant's head without much issue.

The subjective impression about the usability of the two systems let us conclude that the Intersense is much better in capturing posture information. The Kinect has serious problems with a chin rest in view as well (though a chin rest was not used in this study). Due to the nature of the face tracking algorithm, sometimes the lock is lost. We did notice that with visual tracking and debugging tools the Kinect face tracking is perhaps more stable than the Intersense when it has a good tracking lock but this appears to largely be related to very heavy filtering that does not pick up small movements. In fact, it appears that a tracked individual can move their face a bit before the Kinect face tracking updates the pose estimate.

Further products to be mentioned for the same tracking purpose could be the SmartTrack from Advanced Realtime Tracking (ART) [28]. This tracker is suited for tracking within around 2 meters from the camera with 6DOF and sub-millimeter accuracy, but is substantially more expensive. Another straightforward solution could be the Intersense IS900 6DOF tracker [29]. The author also has experience with FaceAPI from Seeing Machines [30] and believes it to be very similar to the performance of the Kinect for Windows with the Microsoft Kinect FaceTracking API.

Hirahara et al. measured spectral deviations of individual HRTFs of three subjects during a 95-minute measurement session [31]. Using the Fastrak sensor they observed excessive head movements in the pitch and yaw directions (up to 10°) but only small movements in the roll (less than 1°). No head fixation was applied, however, subjects were asked to gaze at a fixed point marked on the wall.

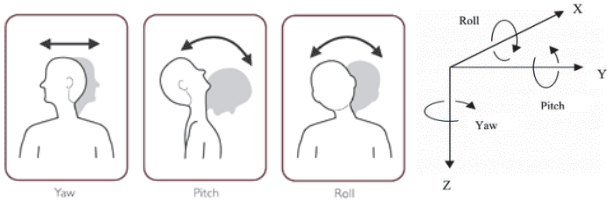

Figure 3. The yaw-pitch-roll coordinate system. Yaw corresponds to azimuth, pitch corresponds to elevation. Intersense and Kinect use a different coordinate system.

Yairi on the other hand reported large head movements in the roll and pitch directions, but small movements in the yaw direction [32]. Both studies reported large head movements after 5 minutes and suggested using head support during HRTF measurements. Table IV and Table V shows the results in signed degree values in the yaw-pitch-roll system (see Fig. 3.) for Intersense and Kinect Face.

Table 4. Result of the Intersense (mean, stdv) in signed degrees.

	mean			std.dev.		
	yaw	pitch	roll	yaw	pitch	roll
StU	2,00	2,02	-0,75	2,23	1,85	0,99
StS	-0,76	2,20	-0,83	1,65	1,59	0,94
SiU	1,32	0,96	-1,18	1,18	1,13	0,70
SiS	0,70	0,23	-0,02	0,80	0,43	0,25

Table 5. Result of Kinect Face Tracking (mean, stdv) in signed degrees.

	mean			std.dev.		
	yaw	pitch	roll	yaw	pitch	roll
StU	-1,15	-0,45	0,53	2,42	2,16	1,82
StS	-0,96	0,01	0,11	2,25	3,20	2,06
SiU	1,60	0,53	0,38	2,77	3,72	1,92
SiS	2,72	2,70	1,08	2,37	3,28	2,22

Our measurement also shows small errors in 3-minute sessions supporting the Japanese results however, standard deviation values are large. Mean measurement differences are defined from the first observed pose in the recorded session. A participant could have a mean measurement near zero and still have a large variance that indicates a lot of movement resulting in large STDV values.

If unsupported, greatest deviations in yaw directions were measured. If supported, differences in pitch can increase. Supported conditions reduce errors in the yaw directions, and partly in pitch and roll as well while seated. Based on the results of Intersense, supported sitting conditions can produce less than 1 degree error in all directions. This position is suggested for measurements however, actual HRTF measurements can be influenced by reflections coming from the legs while sitting. On the other hand, a standing position is uncomfortable and a reflecting wall behind the subject can also influence acoustic tests.

Tables IV and V also indicates large differences (accuracy) between sensors: the Kinect produces larger errors than the Intersense which is definitely the better sensor for this kind of measurements.

In HRTF measurements, 3-5 minute sessions are regarded to be very short. Even using impulse-like excitation, high spatial resolution requires longer recording times from 10-15 minutes up to 60-90 minutes. Our results indicate measurement inaccuracy already after some minutes and thus, breaking down longer measurement periods into shorter sessions is highly recommended if the head is not fixed and/or a rotating chair is used. These parameters introduce more problems to measurement accuracy and an exhaustive study incorporating all these parameters and long measurement sessions is suggested and put for further research.

5. Conclusion

16 subjects participated in a measurement to test different body positions (standing and sitting), different fixation methods (supported and unsupported) and to compare the Intersense and Kinect sensors for data capture. The goal was to determine the extent and variance of body movements if subjects are instructed to be still during individual measurements and recordings. Disagreement with Intersense versus Kinect on which postures allow the participant to be most still was measured. Intersense implies that the order of stillness is: SiS followed by StS or SiU and StU. Kinect head tracking has overlap between sitting and standing. Mean standard deviations of about 1.3-8.4 cm were measured for orientation and head position around the starting position corresponding to about 0-2.20 degrees in all directions. Furthermore, circular angle variance showed very little change between conditions and it was likely that the small unintended movements of the participants were beyond the capabilities of the Kinect to detect. Measurement sessions shorter than 3-5 minutes in a supported sitting situation can result in errors less than 1 degree and less than 2 degrees even in unsupported situations.

Acknowledgement

This research was realized in the frames of TÁMOP 4.2.4. A/2-11-1-2012-0001 „National Excellence Program – Elaborating and operating an inland student and researcher personal support system" The project was subsidized by the European Union and co-financed by the European Social Fund.

This project has received funding from the European Union's Horizon 2020 research and innovation programme under grant agreement No 643636 "Sound of Vision".

References

[1] Blauert J: Spatial Hearing: The Psychophysics of Human Sound Localization. The MIT Press, MA, 1983.
[2] Begault DR: 3-D Sound for Virtual Reality and Multimedia, Academic Press, London, UK, 1994.
[3] Cheng CI, Wakefield GH: Introduction to Head-Related Transfer Functions (HRTFs): Representations of HRTFs in Time, Frequency, and Space. J. Audio Eng. Soc., Vol. 49, pp. 231-249, 2001.
[4] Møller H, Sorensen MF, Hammershøi D, Jensen CB: Head-Related Transfer Functions of human subjects. J. Audio Eng. Soc., Vol. 43, pp. 300-321, May 1995.
[5] Hill PA, Nelson PA, Kirkeby O: Resolution of front-back confusion in virtual acoustic imaging systems. J. Acoust. Soc. Am., Vol. 108, pp. 2901-2910, 2000.
[6] Wightman FL, Kistler DJ: Resolution of front-back ambiguity in spatial hearing by listener and source movement. J. Acoust. Soc. Am., Vol. 105, pp. 2841–2853, 1999.
[7] Perrett S, Noble W: The effect of head rotations on vertical plane localization. J. Acoust. Soc. Am., Vol. 102, pp. 2325–2332, 1997.
[8] Wenzel EM: Localization in virtual acoustic displays. Presence, Vol. 1, pp. 80–107, 1991.

[9] Sandvad J: Dynamic aspects of auditory virtual environments. 100th Convention of the Audio Engineering Society, Copenhagen, Denmark, Preprint 4226, 1996.
[10] Wightman F, Kistler D: Measurement and validation of human HRTFs for use in hearing research. Acta acustica united with Acustica, Vol. 91, pp. 429-439, 2005.
[11] Begault DR, Wenzel E, Anderson M: Direct Comparison of the Impact of Head Tracking Reverberation, and Individualized Head-Related Transfer Functions on the Spatial Perception of a Virtual Speech Source. J. Audio Eng. Soc., Vol. 49, pp. 904-917, 2001 Oct.
[12] Wenzel EM, Arruda M, Kistler DJ, Wightman FL: Localization using nonindividualized head-related transfer functions. J. Acoust. Soc. Am., Vol. 94, pp. 111-123, 1993.
[13] Møller H, Sorensen MF, Jensen CB, Hammershøi D: Binaural Technique: Do We Need Individual Recordings? J. Audio Eng. Soc., Vol. 44, pp. 451-469, June 1996.
[14] Wersényi Gy: Effect of Emulated Head-Tracking for Reducing Localization Errors in Virtual Audio Simulation. IEEE Transactions on Audio, Speech and Language Processing, Vol. 17, pp. 247-252, Feb 2009.
DOI: 10.1109/TASL.2008.2006720
[15] Van Dijk KR, Sabuncu MR, Buckner RL: The influence of head motion on intrinsic functional connectivity MRI. NeuroImage, Vol. 59, No. 1, pp. 431–438, January 2012.
DOI: 10.1016/j.neuroimage.2011.07.044
[16] Thesen S, Heid O, Mueller E, Schad LR: Prospective acquisition correction for head motion with image-based tracking for real-time fMRI. Magnetic Resonance in Medicine, vol. 44, no. 3. pp. 457–465, September 2000.
DOI: 10.1002/1522-2594(200009)44:3<457::AID-MRM17>3.0.CO;2-R
[17] Forbes KPN, Pipe JG, Bird C, Heiserman JE: PROPELLER MRI: Clinical testing of a novel technique for quantification and compensation of head motion. Journal of Magnetic Resonance Imaging, Vol. 14, No.3. pp. 215–222, September 2001.
DOI: 10.1002/jmri.1176
[18] Menke M, Atkins MS, Buckley KR: Compensation methods for head motion detected during PET imaging. IEEE Transactions on Nuclear Science, Vol. 43, No. 1, pp. 310 – 317, Feb. 1996.
DOI: 10.1109/23.485971
[19] Green MV, Seidel J, Stein SD, Tedder TE, Kempner KM, Kertzman C, Zeffiro TA: Head movement in normal subjects during simulated PET brain imaging with and without head restraint. J. Nuc. Med., Vol. 35, pp. 1538 -1546, 1994.
[20] Basu S, Essa I, Pentland A: Motion regularization for model-based head tracking. Pattern Recognition, Vol. 3, pp. 611-616, Vienna, Austria, 25-29 Aug. 1996.
DOI: 10.1109/ICPR.1996.547019
[21] Pentland A, Horowitz B: Recovery of nonrigid motion and structure. IEEE Trans. Pattern Analysis and Machine Intelligence, Vol. 13, No. 7, pp. 730-742, 1991.
DOI: 10.1109/34.85661

[22] Azuma R, Bishop G: A frequency-domain analysis of head-motion prediction. Proc. of SIGGRAPH '95 - 22nd Conf. on Computer Graphics and Interactive Techniques, pp. 401-408, 1995.
DOI: 10.1145/218380.218496
[23] So RHY, Griffin MJ: Compensating Lags in Head-Coupled Displays Using Head Position Prediction and Image Deflection. Journal of Aircraft, Vol. 29, No. 6, pp. 1064-1068, November-December 1992.
DOI: 10.2514/3.46285
[24] Blauert J: Untersuchungen zum Richtungshören in der Medianebene bei fixiertem Kopf, PhD dissertation, Techn. Hochschule Aachen, Germany, 1969.
[25] Brungart DS, Simpson BD, McKinley RL, Kordik AJ, Dallman RC, Ovenshire DA: The interaction between head-tracker latency, source duration, and response time in the localization of virtual sound sources. Proc. of the 10th Int. Conf. on Auditory Display, Sydney, Australia, pp 1-7, July 6-9, 2004.
[26] http://www.intersense.com/pages/18/11/
[27] http://www.microsoft.com/en-us/kinectforwindows/
[28] http://www.ar-tracking.com/products/tracking-systems/smarttrack/
[29] http://www.intersense.com/pages/20/14
[30] http://www.seeingmachines.com/product/faceapi/
[31] Hirahara T, Sagara H, Toshima I, Otani M: Head movement during head-related transfer function measurements. Acoust. Sci. & Tech., Vol. 31, No. 2, pp. 165-171, 2010.
DOI: 10.1250/ast.31.165
[32] Yairi S: A study on system latency of virtual auditory display responsive to head movement. PhD dissertation, Tohoku University, (in Japanese) 2006.

Acta
Technica
Jaurinensis

Vol. 8, No. 3, pp. 230-239, 2015
DOI: 10.14513/actatechjaur.v8.n3.375
Available online at acta.sze.hu

Estimating the Thermal Bridge at Wall Corners with Artificial Neural Network

M. Orosz, J.E. Csanaky

**Budapest University of Techncology and Economics,
Department of Construction Materials and Technologies
Műegyetem rkp. 3, H-1111 Budapest, Hungary
Phone: +36 1 463 1539
e-mail: orosz.mate@epito.bme.hu**

Abstract: Nowadays there are several software products to simulate the heat transfer at thermal bridges. These sophisticated tools are mostly based on Finite Difference or Finite Element Methods. However, there is a demand from energy modelers to estimate the linear thermal transmittance and the lowest internal surface temperature from existing data, instead of employing time-consuming simulations for each case. This paper investigates wall corners with and without thermal insulation by using Artificial Neural Network (ANN), as a Soft Computing technique. It gives simple formulas that estimate the thermal bridge at wall corners with an acceptable level of accuracy.

Keywords: thermal bridge, linear thermal transmittance, artificial neural network, radial basis function

1. Introduction

Thermal bridges have a significant effect on energy performance and comfort of buildings, therefore their investigation during the design phase is inevitable. In case of high performance buildings thermal bridges' relative contribution to transmission heat loss is even greater [17]. Moreover, moisture condensation at thermal bridges is one of the mean reasons for physical degradation of building constructions [18].

The variables describing this phenomenon are the linear thermal transmittance (Ψ) [W/mK], measuring heat loss, and the lowest internal surface temperature (Θ), indicating possible moisture condensation. To calculate these values, different building energy software products are available, e.g. Therm 7, Heat 3, heat transfer module of Comsol Multiphysics etc. [1, 14, 15]. These mostly apply numerical methods (Finite Difference Method (FDM) or Finite Elements Method (FEM)) to approximate the heat transfer through the building envelope. However, in practice, simpler and less expensive estimations are needed. There are spreadsheets available for many previously investigated cases [5], but the numerous possible building materials and design options demand a new approach.

A thermal bridge can be described by a multivariable function, where independent variables are the physical and geometrical properties of building elements, such as thickness and thermal conductivity; and dependent variables are the linear thermal transmittance (Ψ) and the lowest (dimensionless) temperature of the internal surface (Θ) [4, 6].

Numerical simulations are carried out for many cases [5], and similar cases can be interpolated from these results. However; in this paper, instead of interpolating from existing data, functions describing the phenomenon are approximated. The most common applicable techniques to estimate an unknown function are polynomial and rational function approximations, both having advantages and disadvantages. Polynomial models have a simple form, and with sufficiently high degree of its term, it approximates the target function accurately. However, it has poor generalization capability (overlearning, Runge phenomena) [19]. Rational function approximation has better generalization properties, however it is less known by engineers.

Recently, Soft Computing techniques have also been used for modelling input-output relations. This field of computer science, which emerged in the early 1990s, includes several sub-fields such as Probabilistic Models, Fuzzy Systems, Evolutionary Algorithms and Artificial Neural Networks (ANN). According to the universal approximation theorem, a multilayer feed-forward neural network is deemed a universal approximator [3, 12, 20], since it has the ability to approximate any continuous function with arbitrary precision. In this paper a neural network model is developed by using the Neural Network application of Wolfram Mathematica [16].

2. Methodolgy

In this research Radial Basis Function (RBF) Network is applied to approximate the unknown function [2], since it is the most promising neural network model for data approximation [11]. Fig. 1. shows an RBF Network with inputs $x_1, \ldots, x_k$ and output $\hat{y}$.

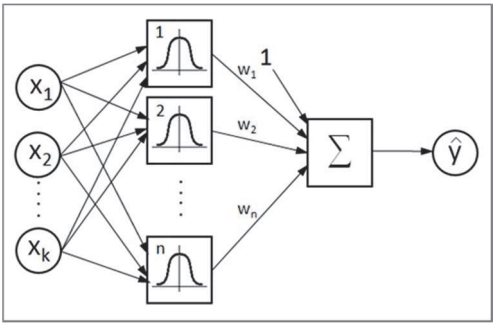

Figure 1. RBF network with one output

The arrows in the figure represent the information-flow in the network. It consists of one hidden layer, where the basis functions are usually Gaussian bell shaped curves (1) with two parameters (λi, βi):

$$e^{-\lambda^2(x-\beta)^2} \tag{1}$$

The output is formally expressed in equation (2):

$$\hat{y}(\theta) = g(\theta, x) = \sum_{i=1}^{n} w_i e^{-\lambda_i^2 (x-\beta_i)^2} + w_{n+1} + \chi_1 x_1 + \ldots + \chi_k x_k \qquad (2)$$

where n is the number of neurons, each neuron contains an RBF type activation function. The parameters (wi, βi, λi) are tuned so that the training data fit the network output in least square sense [10]. The RBF network usually contains a linear part as well, its parameters are $\chi_1,\ldots,\chi_k$. The output is formed by the weighted sum of the neuron outputs, the bias (w_{n+1}) and the optional linear part. An RBF network can be multi-output as well, as our research demonstrates it.

3. Data Preparation

In this paper two types of wall corners are investigated (see Fig. 2.). The first one is not insulated; the other one contains continuous, external thermal insulation. The thermal transfer was simulated previously with ANSYS 11 and HEAT3 Version 5.0. [5]. The data sets for neural networks are composed from these simulation results.

The first data set consists of 106 vectors, each containing 4 elements: width of wall (M_{wall} = 20, 25, 28, 30, 40, 50, 60, 65, 70, 75 cm), thermal conductivity (λ_{wall} = 0.05 – 0.90 W/mK) as input; linear thermal transmittance (Ψ = 0.015 – 0.307 W/mK), and the lowest internal surface temperature in case of 1°C air temperature difference (Θ = 0.460 – 0.941) as output.

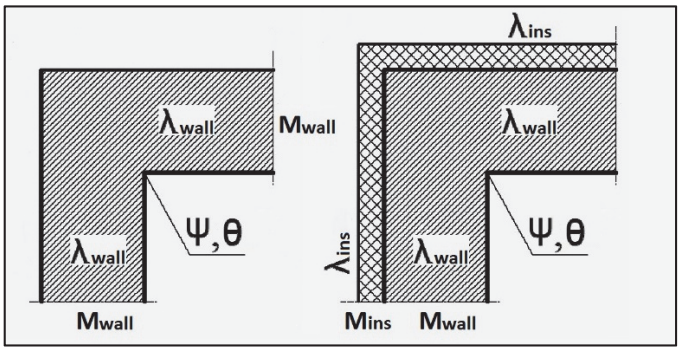

Figure 2. Investigated wall corners (non-insulated and with continuous thermal insulation)

A neural network requires a training set, which, in the first case, contains two-thirds of all the vectors. This training set fulfils certain requirements, i.e. every point being at the boundary is in the training set in order to avoid inaccuracy caused by extrapolation; and the training points are evenly distributed as well. In order to check the accuracy of the network, a validation set is also established containing the rest of the points (see Fig. 3.).

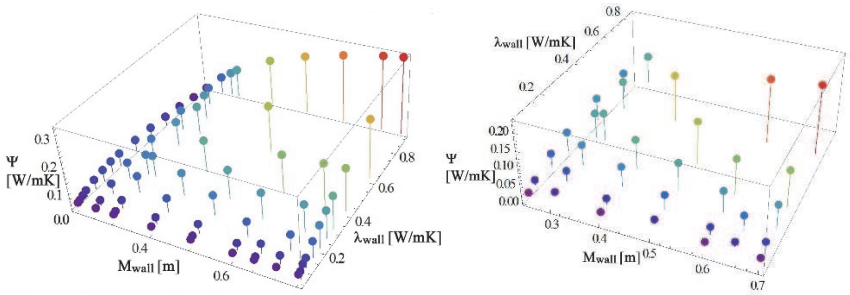

Figure 3. Training set (left) and the validation set (right) for the linear thermal transmittance (Ψ) at non-insulated wall corners

In the second case, when the wall corner is insulated, there are more possible combination of physical properties. Therefore, more simulation data (340) are used, each representing a possible combination of thickness and thermal conductivity of the wall as well as the thermal insulation. These data compose the input (M_{wall} = 20, 40, 60, 80 cm; λ_{wall} = 0.1 – 3 W/mK, M_{ins} = 0, 5, 10, 20, 40 cm, λ_{ins} = 0.02 – 0.10 W/mK). The output has two components: the linear thermal transmittance (Ψ = 0.025 – 4.360 W/mK), and the lowest internal surface temperature in case of 1°C air temperature difference (Θ = 0.430 – 0.990). In this model there is no validation set, all the data are used for training in order to reach the most accurate result. (The ultimate goal is to utilize the analytical form of the result to create a simple calculator tool for engineers.)

The input data are normalized into [0,1] interval in both cases in order to increase the sensitivity of the network; i.e. a larger gradient section of the activation function is used during teaching the neural network.

4. Results

In case of the non-insulated corner, 4 active neurons are used during the initialization of the network (see Fig. 4.). The training time is set to maximum 500 iterations, it stops at 66 iterations (see Fig. 5.).

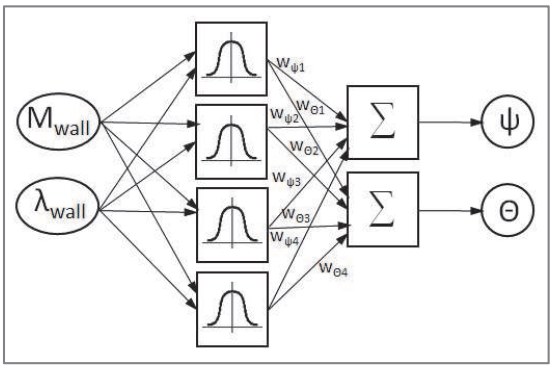

Figure 4. Neural network model – Non-insulated wall corner (n=4 active neurons)

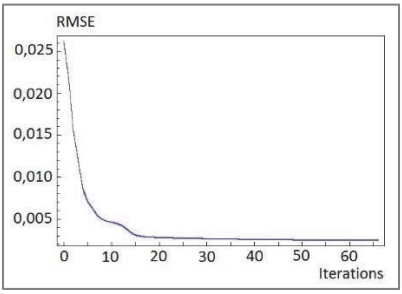

Figure 5. Root-mean-square-error during learning (Ψ) – Non-insulated wall corner

After the learning process, the output i.e. the linear thermal transmittance (Ψ) and the internal surface temperature (Θ) can be expressed in analytical form by equations (3) and (4):

$$\psi_{wall} = A_{\psi} - \sum_{i=1}^{4} w_{\psi_i} e^{-\alpha_i (c_i + C(-M_{wall.min} + M_{wall}))^2 - \alpha_i (d_i + D(-\lambda_{wall.min} + \boldsymbol{\lambda_{wall}}))^2} + \\ + \chi_{\psi 1}(-M_{wall.min} + M_{wall}) + \chi_{\psi 2}(-\lambda_{wall.min} + \lambda_{wall}) \quad (3)$$

$$\Theta_{wall} = A_{\Theta} + \sum_{i=1}^{4} w_{\Theta_i} e^{-\alpha_i (c_i + C(-M_{wall.min} + M_{wall}))^2 - \alpha_i (d_i + D(-\lambda_{wall.min} + \boldsymbol{\lambda_{wall}}))^2} + \\ + \chi_{\Theta 1}(-M_{wall.min} + M_{wall}) + \chi_{\Theta 2}(-\lambda_{wall.min} + \lambda_{wall}) \quad (4)$$

where A_{Ψ}, A_{Θ}, C, D, $\chi_{\Psi 1}$, $\chi_{\Psi 2}$, $\chi_{\Theta 1}$, $\chi_{\Theta 2}$ are constants; $w_{\Psi i}$, $w_{\Theta i}$, α_i, c_i, d_i parameters are tuned so that the training data fit the network output in least square sense. The root-mean-square-error (RMSE) is less than 0.005 (see Fig. 5). The constant and variable parameters are summarized in Table 1. and Table 2.

Table 1. Constant parameters in case of n=4 active neurons – Non-insulated wall corner

A_{Ψ}	A_{Θ}	C	D	$\chi_{\Psi 1}$	$\chi_{\Psi 2}$	$\chi_{\Theta 1}$	$\chi_{\Theta 2}$
-3.31449	+7.39351	+1.81818	+1.17647	-3.97787	+0.554254	+7.37195	-1.52399

Table 2. Variable parameters in case of n=4 active neurons – Non-insulated wall corner

Neuron	$w_{\Psi i}$	$w_{\Theta i}$	α_i	c_i	d_i
1.	-2.99089	+0.632	-1.58735	+1.27706	-1.04001
2.	+253.188	-476.098	-0.335266	-1.61557	-1.03893
3.	-994.824	+1900.52	-0.30733	-1.65803	-0.961438
4.	+749.15	-1438	-0.296573	-1.67726	-0.930631

Plotting the graph of the functions, Ψ_{wall} and Θ_{wall} surfaces perfectly fit the training points (see Fig 6.). As for the validation set, a slightly worse, but still remarkable coincidence can be seen (see Fig 7.). Notice, that the extrapolation capability of the model is weak, thus the applicable domain of new points should be within the convex hull of input points.

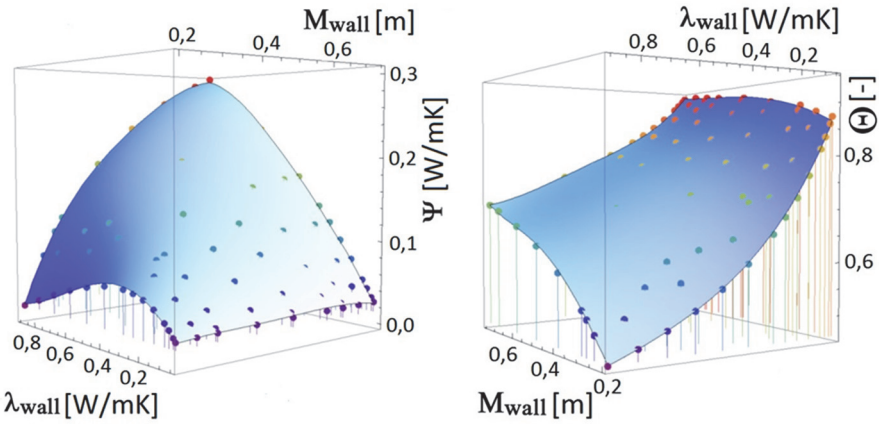

Figure 6. RBF network models of Ψ (left) and Θ (right), and the training points

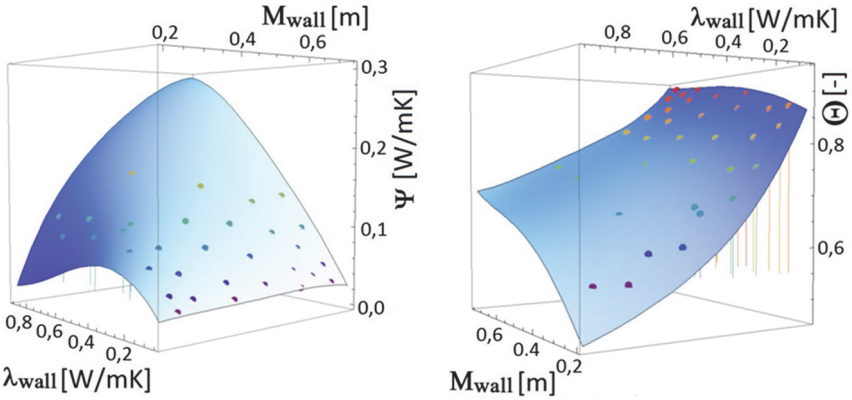

Figure 7. RBF network models of Ψ (left) and Θ (right), and the validation points

The maximum deviation of the thermal transmittance and the lowest internal surface temperature from simulated data are summarized in Table 3. Since the MSZ EN ISO 14683:2008 standard [13] provides data for simple cases of thermal bridges with a precision of 0.01, the accuracy of results for the training set is acceptable; however, for the validation set the approximation would require higher accuracy. This can be reached by applying more active neurons or having more points in the training set.

Table 3. Maximum deviation from simulated data – Non-insulated wall corner

DATA SET	**Linear thermal transmittance (Ψ) [W/mK]**	**Lowest internal surface temperature (Θ) [-]**
Training set	0.0056 (6.55%)	0.0082 (0.94%)
Validation set	0.0565 (64.72%)	0.0695 (12.68%)

In case of the insulated wall corner, the initialization of the longer data vector and more input data demand more neurons: a hidden layer with 40 neurons gives optimal accuracy (see Fig. 8.).

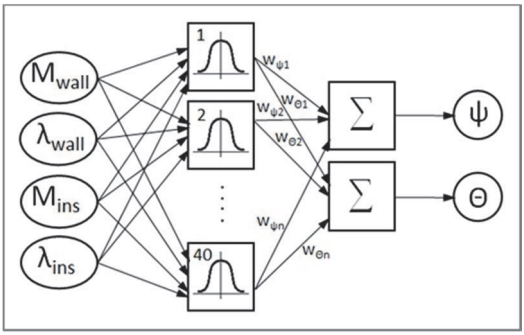

Figure 8. Neural network model – Insulated wall corner (n=40 active neurons)

After the training process, which is also longer with 600 iterations, the root-mean-square-error (RMSE) is less than 0.01. The results, the linear thermal transmittance and the internal surface temperature can be expressed in analytical form by equations (5) and (6):

$$\psi_{wall} = = A_{\psi} + \sum_{i=1}^{40} w_{\psi_i} e^{-\alpha_i(c_i+C(-M_{wall.min}+M_{wall}))^2-\alpha_i(d_i+\frac{M_{ins}}{M_{ins.max}})^2-\alpha_i(f_i+F(-\boldsymbol{\lambda_{wall.min}}+\boldsymbol{\lambda_{wall}}))^2-\alpha_i(g_i+\frac{\boldsymbol{\lambda_{ins}}}{\boldsymbol{\lambda_{ins.max}}})^2} + \chi_{\psi 1}(-M_{wall.min}+M_{wall}) + \chi_{\psi 2}\frac{M_{ins}}{M_{ins.max}} + \chi_{\psi 3}(-\lambda_{wall.min}+\lambda_{wall}) + \chi_{\psi 4}\frac{\lambda_{ins}}{\lambda_{ins.max}} \quad (5)$$

$$\Theta_{wall} = = A_{\Theta} + \sum_{i=1}^{40} w_{\Theta_i} e^{-\beta_i(c_i+C(-M_{wall.min}+M_{wall}))^2-\beta_i(h_i+\frac{M_{ins}}{M_{ins.max}})^2-\beta_i(j_i+F(-\boldsymbol{\lambda_{wall.min}}+\boldsymbol{\lambda_{wall}}))^2-\beta_i(k_i+\frac{\boldsymbol{\lambda_{ins}}}{\boldsymbol{\lambda_{ins.max}}})^2} + \chi_{\Theta 1}(-M_{wall.min}+M_{wall}) + \chi_{\Theta 2}\frac{M_{ins}}{M_{ins.max}} + \chi_{\Theta 3}(-\lambda_{wall.min}+\lambda_{wall}) + \chi_{\Theta 4}\frac{\lambda_{ins}}{\lambda_{ins.max}} \quad (6)$$

each containing 7 constant and 6 variable parameters that are tuned so that the training data fit the network output in least square sense.

The maximum deviations from simulated data are 0.0043 [W/mK] for the linear thermal transmittance and 0.0051 [-] for the internal surface temperature (Table 4.), demonstrating that this approximation is also accurate enough [13]. However, deviations differ for each training point, and it might result in significant difference at lower values (below 0.01). The deviations are plotted in Fig. 9.

Table 4. Maximum deviation from simulated data – insulated wall corner

DATA SET	**Linear thermal transmittance (Ψ) [W/mK]**	**Lowest internal surface temperature (Θ) [-]**
Training set	0.0043	0.0051

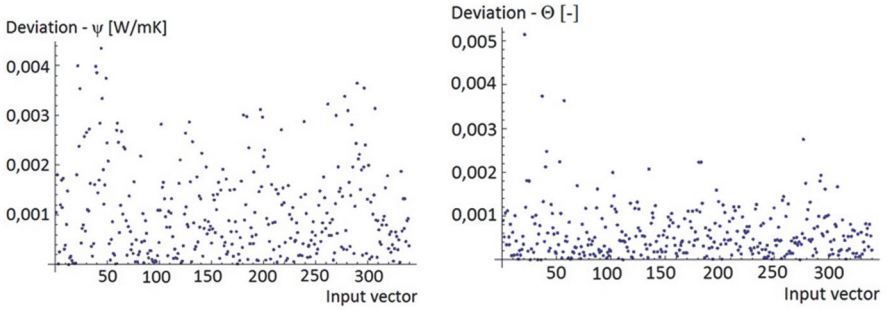

Figure 9. Deviation from simulated data
Insulated wall corner, Ψ [W/mK] (left), Θ [-] (right)

5. Conclusions

This paper seeks a new method to approximate the function describing the thermal bridge at wall corners by using Artificial Neural Network modelling. The model uses data of physical properties (thickness, thermal conductivity), and results of previously conducted simulations (linear thermal transmittance - Ψ, and the lowest internal surface temperature - Θ). Activation functions are radial basis functions (RBF), since it was found the most efficient for this purpose. The paper demonstrates, that in case of a non-insulated wall corner less active neurons (4 active neurons per 106 input data) give an acceptable precision for training data; however, for an insulated wall corner, the more possible combinations of physical properties require more active neurons (40 active neurons per 340 input data). The paper also shows, that the validation set should be chosen thoroughly, since it can have an impact on results: points at the boundary should not be in the

validation set; and having more points in the validation set i.e. less points in the training set decreases the overall accuracy.

Besides the advantages of this technique, there are some weaknesses as well. Due to the weak extrapolation capability of this method, the physical properties of the investigated thermal bridge must be within the domain of training data. Furthermore, the deviations from the simulated data vary, and it might result in significant difference at lower input values. However, the target function can be approximated with arbitrary precision by increasing the number of active neurons and/or the number of training points.

After the training process the results can be expressed in analytical form that are easily exportable into other software products (e.g. Microsoft Excel) to create a simple calculator for engineers. Further research is suggested, during which input data are considered stochastic variables and the histogram of the output is produced by Monte-Carlo simulation.

Acknowledgement

The authors are grateful to Dr. Béla Paláncz (BME) and Sean McMahon (USGBC) for their valuable feedback and peer review.

References

[1] Blomberg, T: Heat conduction in two and three dimensions, Computer Modelling of Building Physics Applications. Lund: Dept. of Building Physics, Lund University, Sweden, ISBN 91-88722-05-8, 1996.

[2] Broomhead, DS., Lowe, D,: Multivariable function interpolation and adaptive networks. Complex Systems, Vol. 2, pp 321-355, 1988. Available at: http://sci2s.ugr.es/keel/pdf/algorithm/articulo/1988-Broomhead-CS.pdf, (accessed 31 March 2015), 1988.

[3] Csáji, CsB.: Approximation with Artificial Neural Networks. MSc Thesis, Faculty of Sciences, Eötvös Loránd University, Hungary, 2001.

[4] Csanaky, JE: A legegyszerűbb geometriai hőhíd – a derékszögű falsarok. Magyar Építőipar 2009: (3) pp. 107-110, 2009.

[5] Csanaky, JE: Épületszerkezetek energiatudatos fejlesztése az építészeti és épületfizikai tervezés határfelületén. PhD Thesis, Széchenyi István University, Győr, 2012.

[6] Csanaky, JE: Wall-corner – the simplest type of thermal bridges. Acta Technica Jaurinensis, 3: Paper B113, 2010.

[7] EN ISO 10211:2007 Thermal bridges in building construction – Heat flows and surface temperatures – Detailed calculations (ISO 10211:2007). Brussels: CEN, 2007.

[8] EN ISO 10456:2007 Building materials and products – Hygrothermal properties – Tabulated design values and procedures for determining declared and design thermal values. Brussels: CEN, 2007.

[9] EN ISO 6946:2007 Building components and building elements – Thermal resistance and thermal transmittance – Calculation method (ISO 6946:2007). Brussels: CEN, 2007.

[10] Freeman JA: Simulating Neural Networks with Mathematica, Addison Wesley, ISBN: 020156629X, New York, 1994.
[11] Haykin I: Neural Networks: A Comprehensive Foundation, Second Edition, Macmillan, New York, 1999.
[12] Hornik, K, Stinchcombe, M, White, H: Multilayer feedforward networks are universal approximator, Neural Networks, Vol. 2, 1989: (5), pp 359-366, Available at: http://deeplearning.cs.cmu.edu/pdfs/Kornick_et_al.pdf (accessed 31 March 2015), 1989.
DOI: 10.1016/0893-6080(89)90020-8
[13] MSZ EN ISO 14683:2008 Hőhidak az épületszerkezetekben. Vonal menti hőátbocsátási tényező. Egyszerűsített módszerek és felülírható kiindulóértékek (ISO 14683:2007), 2008.
[14] Nagy, B: Comparative analysis of multi-dimensional heat flow modeling, In: Cosmin G Chiorean (ed.), Proceedings of the Second International Conference for PhD Students in Civil Engineering and Architecture: Full papers. Place and date of conference: Cluj-Napoca, Romania, 10/12/2014-13/12/2014. Cluj-Napoca: Editura UTPress, pp. 468-476, 2014.
DOI: 10.13140/2.1.2666.4003
[15] Nagy, B: Geometriai modellek kialakításának hatása tetőcsomópontok végeselemes és véges differenciamódszeres többdimenziós hőtechnikai szimulációi esetén. Magyar Építőipar 2014:(5) pp. 202-205, 2014.
[16] Neural Network Documentation, Available at: http://reference.wolfram.com/applications/neuralnetworks/ (accessed 10 February 2013), 2013.
[17] Olsen, L, Radisch, N: Thermal bridges in residential building in Denmark. Brno: KEA energeticka agentura s.r.o, Czech Republic, ISBN 80-902689-6-X, Available at: https://www.tc.cz/files/istec_publications/thermal-bridges.pdf (accessed 8 November 2014), 2002.
[18] Orosz, M: Épületszerkezetek avulása, In: Széll Mária (ed.), Fenntartható energetika az épületszerkezetek tervezésében és oktatásában: Monográfia. 230 p., Budapest: TERC Kereskedelmi és Szolgáltató Kft., 2012. pp. 148-155, ISBN 978-963-9968-32-5, 2012.
[19] Paláncz, B, Völgyesi, L: High accuracy data representation via sequence of neural networks. Acta Geodaetica et Geophysica Hungarica Vol. 38, Issue 3, pp. 337-343, Available at: http://sci.fgt.bme.hu/~volgyesi/gravity/neural.pdf (accessed 31 March 2015), 2003.
DOI: 10.1556/AGeod.38.2003.3.4
[20] Zainuddin, Z, Pauline, O: Function approximation using artificial neural networks, School of Mathematical Sciences, Universiti Sains Malaysia, 11800 Minden, Penang, Malaysia, Issue 4, Volume 1, 2007, International Journal of Systems Applications, Engineering & Development 2007:4, Vol 1, Available at: http://ww.naun.org/multimedia/UPress/saed/saed-23.pdf (accessed 8 November 2014), 2007.

Acta
Technica
Jaurinensis

Vol. 8, No.3, pp. 240-256, 2015
DOI: 10.14513/actatechjaur.v8.n3.384
Available online at acta.sze.hu

Traction Energy Consumption of Electric Locomotives and Electric Multiple Units at Speed Restrictions

Sz. Fischer

Széchenyi István University, Department of Transport Infrastructure
Egyetem tér 1, 9026 Győr, Hungary
Phone: +36 30 630 6924
e-mail: fischersz@sze.hu

Abstract: In this article the author reports the measurements made by traction measuring car of Railway Engineering and Metrological Service Centre (REMSC) in the research and development work "Complex investigation of reduction possibilities of additional costs due to speed restrictions on electric traction railway lines". As results it can be stated that α correction parameters in the research and development work made between 2008 and 2010 should be changed because of specifying. These parameters can be used for calculation of additional acceleration energy after speed restriction sites.

Keywords: railway engineering, traction energy consumption, speed restriction, locomotive, EMU

1. Introduction

Analysing electric railway haul there is an important aspect to be considered: speed restrictions will substantially increase traction energy consumption as well as journey time [1,2]. Speed restrictions are needed because of transport safety due to railway track faults as well as cancelling of these railway track faults' elimination [3,4,5]. In case of diesel locomotives and diesel multiple units (DMUs) the additional traction energy consumption is related naturally to diesel oil.

There are some other disadvantages due to railway track faults:

- irregular vehicle movements [6,7],
- higher stresses in the elements of railway super- and substructure [3,4,8],
- much faster deterioration process of the railway track in case of cancelling of railway track faults' elimination [4,9].

The author has to mention there are a lot of technologies to avoid track faults or slow down deterioration process that can reduce traction energy consumption in the aspect of railway track, some of them:

- superstructure geometry stabilization with geogrids [10], steel sleepers [11], safety cap and ballast bonding technology [12],
- ballastless superstructure and special railway fastening system [13],
- etc.

There are special methods to decrease total traction energy consumption of the trains publicised in the international literatures. For example recuperated energy can be used and stored more efficiently [14], onboard storage batteries can be utilized for hybrid drive systems [15], onboard ultracaps are useful to energy storage [16]. Fully or partially automated Train Control Systems (TCS) and related operation mathematical algorithms are developed to optimize energy consumption of the trains [17]. Less energy consumption can be reached by target speed optimization [18], and it has to be considered that increased speed influences the wasted energy too [19]. In case of determination of train speed and timetable on the tracks, the difficult sections have to be taken into consideration [20]. These methods are suitable for reducing total traction energy of the trains, but they aren't or only partially adequate for taking into account the energy consumption of the locomotives due to acceleration process after discrete speed restriction.

The research team of Széchenyi István University firstly got research work for exact determination of additional traction energy consumption due to speed restrictions [21,22,23], after that the research and development work was related to comparison of additional traction energy consumption costs and costs of elimination of railway track faults caused by speed restrictions [24].

In the author's [25,26], his pensioner colleague's [22,23] and his research team's previous papers and research reports [21,24] there is an adequate calculation method for determining traction energy consumption of electric locomotives and electric multiple units (EMUs). The α correction parameters are formerly calculated from own energy consumption measurements on locomotives and EMUs, but the used α correction parameters are needed to be specified.

The Hungarian Railways ordered another research and development work from Széchenyi István University in 2011, the topic of this research was the complex analysis of reduction possibilities of additional costs due to speed restrictions on electric haul railway lines. In this research work there are measurements made by traction measuring car of REMSC [27] related to three types of electric locomotives and one type of EMU.

This paper reports the results of new measurements and calculations that belong to traction energy consumption of electric locomotives and EMUs.

2. Necessity and description of measurements made by traction measuring car

In the previous researches of our team calculations can be done only with own measured data on locomotives and EMUs.

These vehicles are the followings:

- Railjet trains hauled by 1116 Siemens Taurus locomotives [28],
- passenger trains hauled by 1047 and 1116 Siemens Taurus locomotives [29],
- freight trains hauled by 1047 and 1116 Siemens Taurus locomotives [29],

- 5341 Stadler Flirt EMU [30],
- 5342 Bombardier Talent EMU [31].

In case total traction energy consumption should be calculated for a determined railway line, correct data are needed for another locomotive too. To get these data additional measurements have to be done. The aim of these measurements is to state the fact that more precise α correction parameters can be used in the calculations which are controlled by traction measurement car.

The simple equations are below:

$$E_{calc} = 0{,}5 \cdot m \cdot \left(v^2 - v_0^2\right) \cdot 3.6 \cdot 10^6 , \tag{1}$$

$$E = \alpha \cdot E_{calc} , \tag{2}$$

where

m – total mass of the train (locomotive and cars) in kg unit,

v and v_0 – values of acceleration speed step in m/s unit,

E – measured electric energy at an acceleration of a locomotive or EMU in kWh unit,

α – correction parameter (factor),

E_{calc} – calculated electric energy after Eq. 1 in kWh unit.

Because of the fact that measurements were done only for Railjet, passenger and freight trains hauled by Taurus locomotives as well as Flirt and Talent EMUs (values of Table 1), α correction parameters for other vehicles are determined by our specialist mechanical engineer colleagues to be able to assume traction energy consumption, these parameters are the followings:

- passenger train hauled by V63-1 (1163) [32]: 1.166,
- freight train hauled by V63-1 (1163) [32]: 1.280,
- passenger train hauled by V43 (1043, 1143, 1243, 1343) [33]: 1.266,
- freight train hauled by V43 (1043, 1143, 1243, 1343) [33]: 1.313,
- passenger train hauled by M41 (2241, 2341) [34]: 1.884,
- freight train hauled by M41 (2241, 2341) [34]: 2.000,
- passenger train hauled by M62-0 (2062) [35]: 1.639,
- freight train hauled by M62-0 (2062) [35]: 1.927,
- 5429 [36] and 6312 [37] EMUs: 1.570.

The goal of the measurement series is to determine α parameter related to several locomotives and passenger as well as freight trains more precisely.

REMSC processed the plan for measurements in October, 2011, after that the measurements were done in April, 2012. Fig. 1. shows the measure train.

Figure 1. Measure train at Öttevény railway station (Ferenc Horvát's photo)

In Fig. 2. there is the set-up of measure train. At the front there is the analysed haul locomotive, behind that there is the VMK–002 [27] traction measuring car, at the back there is a 1047 Siemens Taurus locomotive that brakes the train.

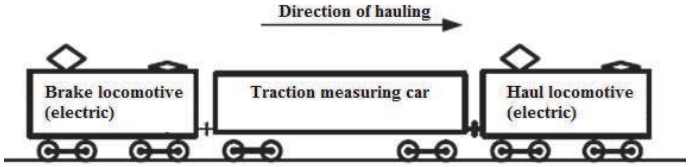

Figure 2. Set-up of measure train

The haul locomotives were the followings in the tests:

- V43 (1338) electric locomotive [33],
- 1047 Siemens Taurus electric locomotive (Taurus) [29],
- V63 (151) electric locomotive [32],
- 5341 (044) Stadler Flirt EMU (Flirt) [30].

Data of the measuring car:

- line number: 60 55 99-80 002-2,
- max. speed: 160 km/h,
- length: 24.5 m,
- weight: 41,000 kg,
- brake mass: 61,000 kg.

Braking simulation was always done with the same 1047 Taurus locomotive. Maximal brake force of this locomotive is 240 kN.

Measure tests were made between railway stations Öttevény and Hegyeshalom on the Hungarian main railway line No. 1. In this section the allowed maximal speed is 160 km/h. The horizontal geometry is quite straight and the vertical geometry does not contain high slopes only quite horizontal sections, as well as the geometrical condition of the track was good, in this way there isn't any distortional effect to energy consumption results.

The final measure program was as below:

- 16th and 17th of April in 2012: measurements with V43 (1338) locomotive, 40-60-80-100-120 km/h constant speed, as well as several speed steps between 40 and 120 km/h,
- 18th and 19th of April in 2012: measurements with Taurus (1047) locomotive, 40-60-80-100-120-140-160 km/h constant speed, as well as several speed steps between 40 and 160 km/h,
- 23rd and 24th of April in 2012: measurements with V63 (151) locomotive, 40-60-80-100-120 km/h constant speed, as well as several speed steps between 40 and 120 km/h,
- 25th and 26th of April in 2012: measurements with Stadler Flirt EMU (5341) locomotive, 40-60-80-100-120-140-160 km/h constant speed, as well as several speed steps between 40 and 160 km/h.

The measurements were made only on the right track in case of V43 and V63 locomotives in the right direction (from Öttevény to Hegyeshalom), but measurements related to Taurus locomotive and Stadler Flirt EMU were made on both tracks always in the right direction.

The REMSC calculated the required traction force values for all the locomotives and EMU for constant speed traction as well as the several speed steps. The required power for traction was determined from the traction force vs. speed diagrams for each measurement cases. Speed restrictions were also simulated (braking, traction with constant speed, acceleration), and electric energy consumption was measured during it. Measurements were done by three several brake forces.

From these data the additional energy consumption could be calculated.

Parameters below were recorded during measurements:

- V – speed in km/h unit,
- s – covered distance in m unit,
- U_p – primer voltage in kV unit,
- I_p – primer amperage in A unit,
- $\cos\phi$ – phase shift,
- P – electric power in kW unit,
- E – energy consumption in kWh unit as the integral of P(t) function,
- F_v – traction force measured on drawbar in kN unit, as well as
- combinated speed and distance signal and the section markers.

In the Fig. 3. several parameters are shown on the display of VMK–002 traction measuring car.

All the measured data can't be published because of limited space of this paper.

Figure 3. Several parameters on the display of VMK–002 traction measuring car

3. Data processing and results of measurements

Measured data from REMSC were processed by calculated specific values, after that specific traction energy data (in kWh/100 m/kN unit) were calculated for each locomotives and EMU. The set brake force values were between 10 and 150 kN (50 kN force simulates passenger train, 100 kN light freight train, and 150 kN heavy freight train). Additional braking wasn't used in case of Stadler Flirt.

During calculation it was supposed that total consumed electric energy was used for transmission of the trains. In case of traction with constant speed the energy equals to the total resistance of the train:

$$E_{used} = Q_{total} \cdot \mu_{train} \cdot s \tag{3}$$

where

E_{used} – consumed electric energy during the travel in kWh unit,

Q_{total} – total weight of the train consideration with brake force in kN unit,

μ_{train} – resistance of the train in N/kN unit,

s – distance that was taken with constant speed in m unit.

The calculation of μ_{train} is presented below in accordance with Hungarian Railways' recommendation from year 1983 [38]:

– in case of passenger train:

$$\mu_{train} = 2 + 0.047 \cdot \frac{V^2}{100} \tag{4}$$

– in case of freight train:

$$\mu_{train} = 2 + 0.057 \cdot \frac{V^2}{100} \tag{5}$$

where

V – speed of the train in km/h unit.

The calculated weight of the train from data of measurements with constant speed is below:

$$Q_{total} = 3.6 \cdot 10^5 \cdot \frac{E_{used}}{\mu_{train} \cdot s} \tag{6}$$

The consumed electric energy equals to the sum of energy against resistance of train and acceleration energy in case of assumed uniform acceleration. The calculated train weight in tons unit is as below [39]:

$$Q_{total} = 3.6 \cdot 10^5 \cdot \frac{E_{used}}{\mu_{train,av.} \cdot s} + 110 \cdot a_{av.} \tag{7}$$

where

$\mu_{train,av.}$ – average of the resistance of the train related to speed values v_1 and v_2 in N/kN unit,

$a_{av.}$ – average acceleration in m/s^2 unit.

Fig. 4. - Fig. 6. show the calculated train weights as a function of set brake forces. The R_2 values in some cases are between 0.5 and 0.75 (weak correlation), but in most cases are between 0.75 and 1.0 (strong correlation).

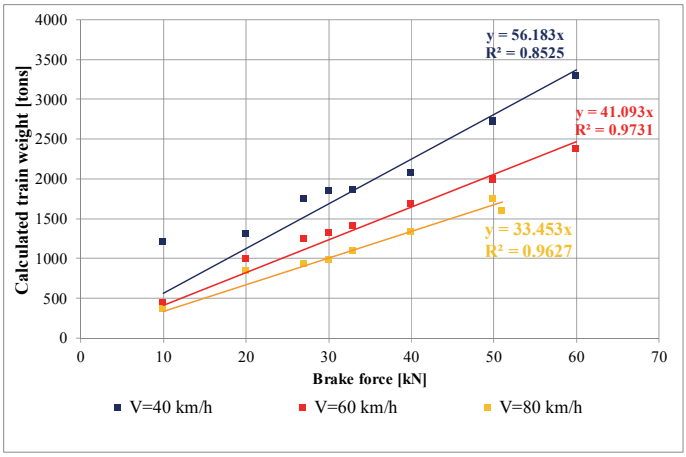

Figure 4. Calculated train weight in case of set several brake forces (V43)

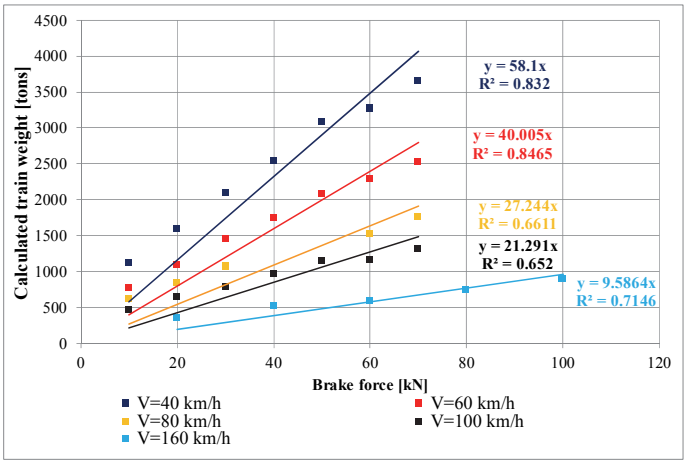

Figure 5. Calculated train weight in case of set several brake forces (Taurus)

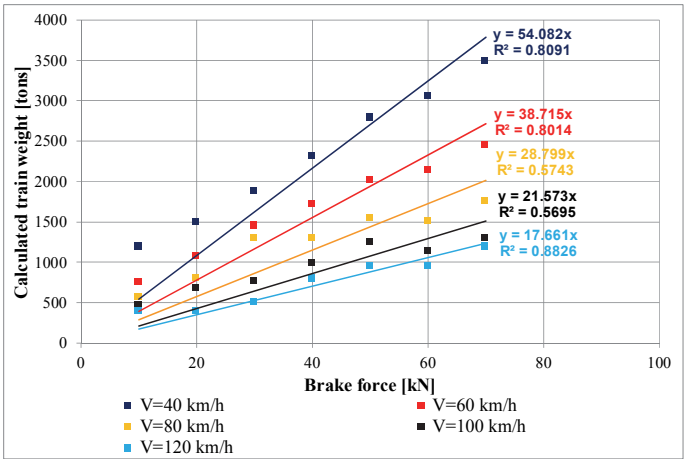

Figure 6. Calculated train weight in case of set several brake forces (V63)

Specific traction energies as a function of train speed are presented in Fig. 7 – Fig. 10. In case of measurements with V43 locomotives the maximum brake force values were 60 kN, in this way freight train diagrams couldn't be made.

Relationship was searched between used and calculated energies (Eq. 1 and Eq. 2).

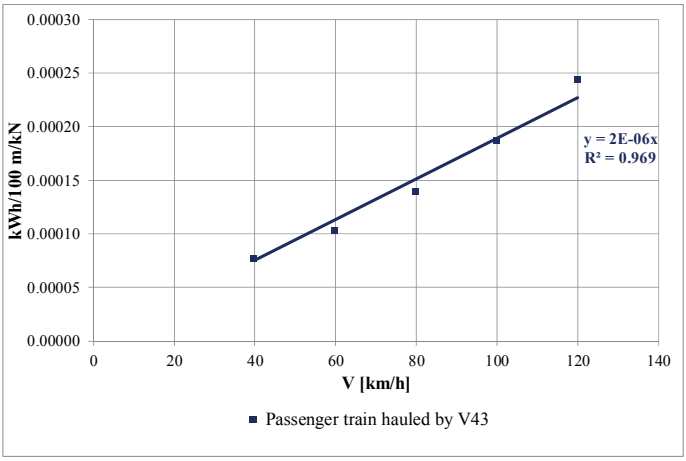

Figure 7. Specified energy consumption of V43 locomotive

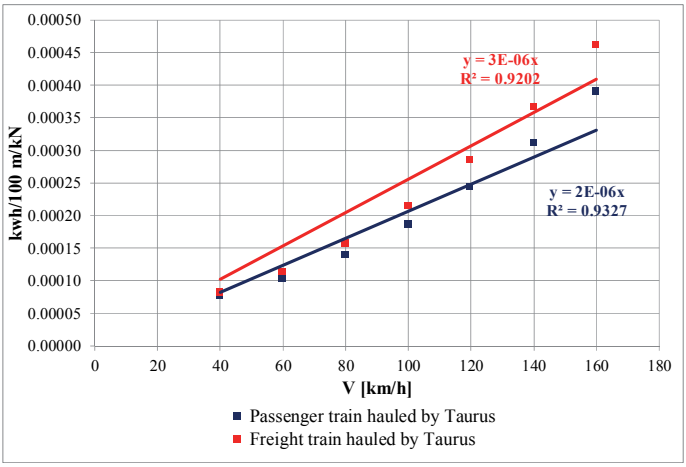

Figure 8. Specified energy consumption of Taurus locomotive

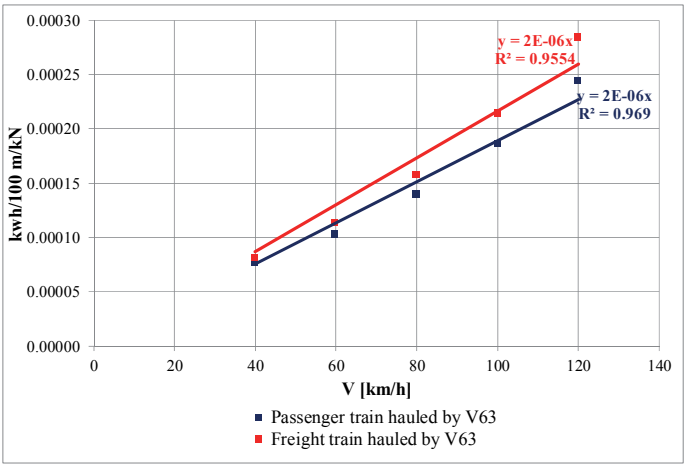

Figure 9. Specified energy consumption of V63 locomotive

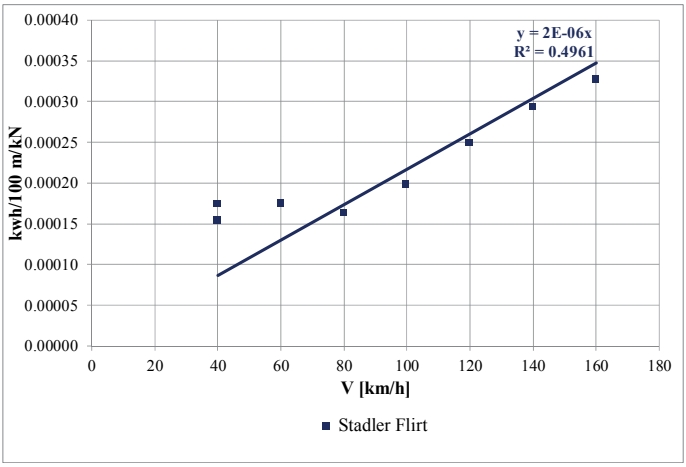

Figure 10. Specified energy consumption of Stadler Flirt EMU

Fig. 11. - Fig. 14. show the electric energy measured by REMSC as a function of calculated energy.

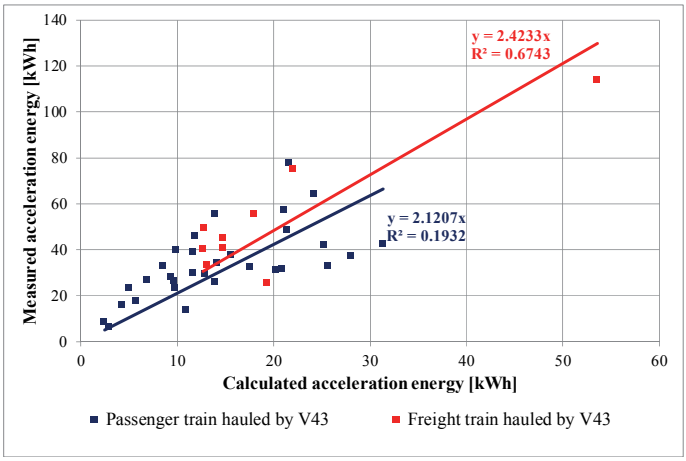

Figure 11. Electric energy measured by REMSC as a function of calculated energy (passenger and freight trains hauled by V43 locomotives)

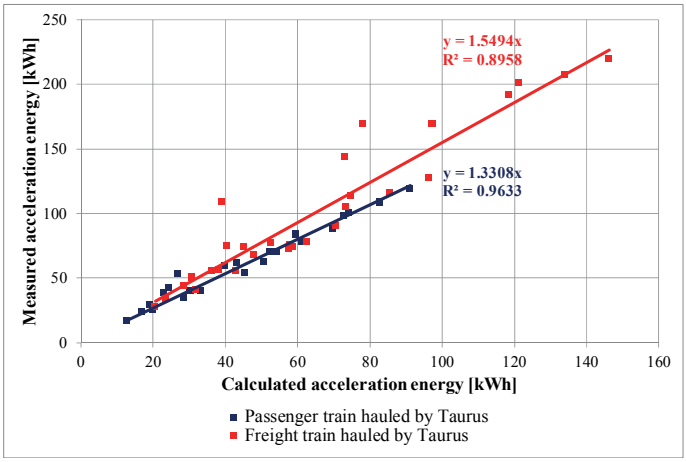

Figure 12. Electric energy measured by REMSC as a function of calculated energy (passenger and freight trains hauled by Taurus locomotives)

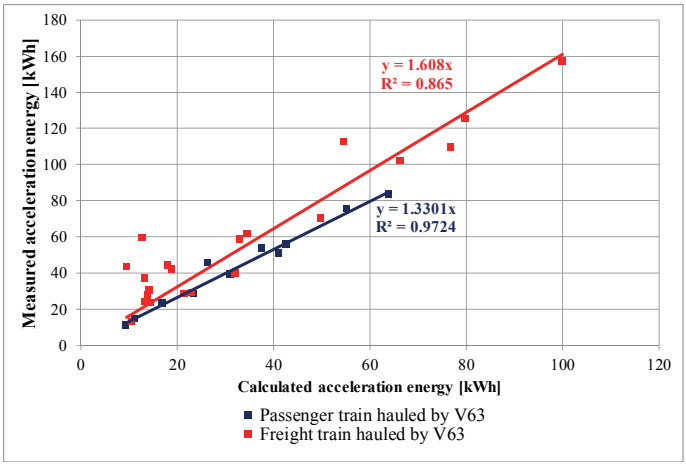

Figure 13. Electric energy measured by REMSC as a function of calculated energy (passenger and freight trains hauled by V63 locomotives)

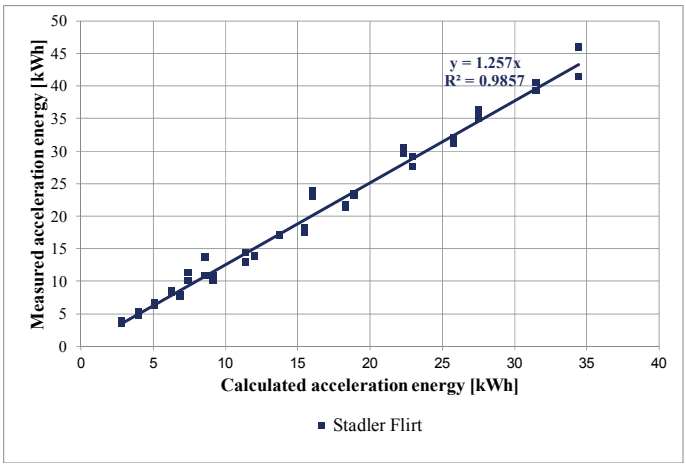

Figure 14. Electric energy measured by REMSC as a function of calculated energy (Stadler Flirt EMU)

Fig. 15. presents the relationship between measured and calculated recuperated energy.

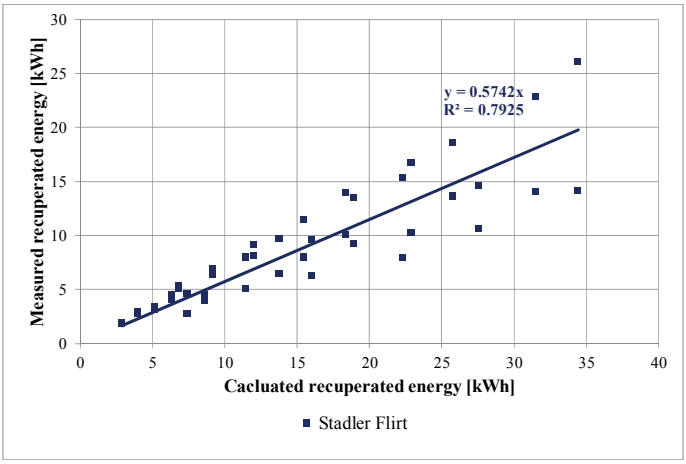

Figure 15. Relationship between measured and calculated recuperated energy (Stadler Flirt EMU)

Comparison of the values measured by REMSC and earlier by our research team is presented in Table 1.

Table 1. Variance of α correction parameters

Type of train	*α*		*Δα*	*Deviation from the values from REMSC measurements (%)*
	From measure-ments by REMSC	*From earlier studies and papers [24,25,26]*		
P. train – Taurus locomotive	1.331	1.415	0.084	6.3
F. train – Taurus locomotive	1.549	1.495	0.054	–3.5
RJ train – Taurus locomotive	–	1.316	–	–
Stadler Flirt EMU	1.257	1.128	0.129	–10.3
Bombardier Talent EMU	–	1.095	–	–
P. train – V43 locomotive	2.121	1.266	0.855	–40.3
F. train – V43 locomotive	2.423	1.313	1.110	–45.8
P. train – V63 locomotive	1.330	1.166	0.164	12.3
F. train – V63 locomotive	1.608	1.280	0.328	20.4

Note: P. train means passenger train, F. train means freight train, RJ means Railjet

4. Evaluation of the data measured by traction measuring car

There isn't significant difference between the theoretical calculated and measured (by REMSC) value of α parameter in case of Taurus locomotive and Stadler Flirt EMU, but there is significant deviation in case of V43 and V63 locomotives. This fact should be answered. The theoretical values were determined in the years 2008 and 2009. That time measurements couldn't be done by these locomotives, correction parameters were calculated assuming new locomotives use special data and diagrams. REMSC made measurements by the V0431 338 locomotive in 2012 which vehicle is older than 30 years. Because of this fact a lot of influencing parameters should be considered:

- the efficiency of traction of V43 locomotive is not the best due to the out of date silicon rectifier,
- the main parts and other accessories aren't the original ones in the locomotives.

Main parts and accessories of V0431 338 locomotive used during the measurements have different lifetime and efficiency, they are in different condition too. 1 % decrease of efficiency of main parts with causes about 3…5 % decrease of whole efficiency of the vehicle.

The first V63 locomotives are ca. 18…20 years younger than V43s. Maintenance strategy is similar to V43's. Because of this fact significant decrease of efficiency can be assumed. This can explain the experienced difference between theoretical and practical values.

Determined correction parameters derived from measurements of REMSC should be used in the future. Parameters from earlier studies are needed to use only in case of Railjet trains and Bombardier Talent EMUs. Because of the fact that there isn't significant difference between correction parameters in Table 1 related to Taurus locomotive, it can be assumed that correction parameter related to Railjet hauled by Taurus is approximately equals to 1.316. This statement may be true in case of Bombardier Talent EMUs.

5. Summary

This paper summarizes the results and evaluation of measurements done by REMSC's traction measuring car related to R&D work financed by Hungarian Railways [40]. Publicised α correction parameters determined in earlier studies could be refined. These more accurate values should be used in case of calculation of additional traction energy consumption due to speed restriction [41].

Acknowledgements

The author and the whole research team thank Dénes Szekeres (MÁV Ltd.), Zsolt Csonka (MÁV Ltd.), Attila Vitéz (MÁV Ltd.), Miklós Simányi (SIU) and the colleagues of MÁV-Trakció Ltd., MÁV-Start Ltd. and REMSC for their help.

References

[1] Kurhan MB, Mukhina NA, Chernyshova OS: The establishment of a rational sequence of the speed restrictions elimination caused by the railway status. Science and Transport Progress. Bulletin of Dnipropetrovsk National University of Railway Transport, No. 25, pp. 72-75, 2008.
[2] Kurhan MB, Muhina NA, Chernyshova OS: The forecasting effort changes in traction energy of metrics at any speed. Science and Transport Progress. Bulletin of Dnipropetrovsk National University of Railway Transport, No. 27, pp. 121-124, 2009.
[3] Lichtberger B: Track compendium. Eurailpress Tetzlaff-Hestra GmbH & Co. KG, Hamburg, 634 p, 2005.
[4] Esveld C: Modern railway track, MRT-Production. Zaltbommel, 723 p, 2001.
[5] Kurhan MB, Zaiats MA: Efficiency determination of freight and passenger traffic division according to the expenses criteria for superstructure maintenance and repair. Science and Transport Progress. Bulletin of Dnipropetrovsk National University of Railway Transport, No. 35, pp. 99-105, 2010.
[6] Iwnicki S (ed.): Handbook of railway vehicle dynamics. CRC Taylor & Francis Group, Boca Raton, 535 p, 2006.
[7] Knothe K (ed.), Grassie St.L (ed.), Elkins JA (ed.): Interaction of railway vehicles with the track and its substructure. CRC Taylor & Francis Group, New York, 390 p, 2007.
[8] Kurhan DM: Features of perception of loading elements of the railway track at high speeds of the movement. Science and Transport Progress, Bulletin of Dnipropetrovsk National University of Railway Transport, No. 2, pp. 136-145, 2015.
[9] Robinson M (ed.), Kapoor A (ed.): Fatigue in railway infrastructure. CRC Woodhead Publishing Limited, Padstow, Cornwall, 114 p, 2009.
[10] Horvát F, Fischer Sz, Major Z: Evaluation of railway track geometry stabilisation effect of geogrid layers under ballast on the basis of laboratory multi-level shear box tests. Acta Technica Jauriensis, Vol. 6, No. 2, pp. 21-44, 2013.
[11] Liegner N: Investigation of the internal forces of the first track constructed with Y-shape steel sleepers under operation in Hungary. Periodica Polytechnica: Civil Engineering, No. 1-2, pp. 115-130, 2004.

[12] Szabó J: Tests experiences in small radius curves of continuously welded rail tracks. Periodica Polytechnica: Civil Engineering, No. 2, pp. 177-189, 2011. DOI: 10.3311/pp.ci.2011-2.10
[13] Major Z: Longitudinal Behaviour of Embedded Rails. Acta Technica Jauriensis, Vol. 8, No. 2, pp. 179-187. 2015. DOI: 10.14513/actatechjaur.v8.n2.367
[14] Kondo K: Recent Energy Saving Technologies on Railway Traction Systems. IEEJ Transactions on Electrical and Electronic Engineering, No. 5, pp. 298-303, 2010. DOI: 10.1002/tee.20533
[15] Shimada M, Miyaji Y, Kaneko T, Suzuki K: Energy-saving Technology for Railway Traction Systems Using Onboard Storage Batteries. Hitachi Review, No. 7, pp. 312-318, 2012.
[16] Steiner M, Klohr M, Pagiela S: Energy storage system with ultracaps on board of railway vehicles. Power Electronics and Applications, 2007 European Conference on, Aalborg, 2-5 Sept. pp. 1-10, 2007. DOI: 10.1109/EPE.2007.4417400
[17] Liu R, Golovitcher IM: Energy-efficient operation of rail vehicles. Transportation Research Part A: Policy and Practice, No. 10, pp. 917-932, 2003. DOI: 10.1016/j.tra.2003.07.001
[18] Feng X: Optimization of target speeds of high-speed railway trains for traction energy saving and transport efficiency improvement. Energy Policy, No. 12, pp. 7658-7665, 2011. DOI: 10.1016/j.enpol.2011.08.051
[19] Korzhenevych IP, Kurgan MB, Barash YuS, Kurhan DM: The impact of the increased speed of trains on wasted energy. Science and Transport Progress. Bulletin of Dnipropetrovsk National University of Railway Transport, No. 20, pp. 233-239, 2008.
[20] Kurhan MB, Kurhan DM, Khmelevska NP, Baidak S.YU: Methodology of determination of admissible speeds of train movement on difficult sections of railroad plan. Science and Transport Progress. Bulletin of Dnipropetrovsk National University of Railway Transport, No. 2, pp. 83-94, 2014.
[21] Universitas-Győr Nonprofit Kft.: A vasúti pályán a lassújelek után szükséges gyorsítások energiaigényének vizsgálata. Research report, Győr, 152 p, 2009.
[22] Kiss F: A vasúti pálya lassújelei okozta vontatási többletenergiák és költségeik. XIII. Nemzetközi Építéstudományi Konferencia, Csíksomlyó, Romania, June 11-14, pp. 237-245, 2009.
[23] Kiss F: A vasúti pálya lassújelei okozta vontatási többletenergiák és költségeik, Közlekedésépítési Szemle, No. 6, pp. 10-16, 2009.
[24] Universitas-Győr Nonprofit Kft.: Lassújelek okozta vontatási energiatöbblet költségeinek és a lassújelet okozó pályahiba kijavítási költségeinek összevetése. Research report, Győr, 199 p, 2010.
[25] Fischer Sz: Lassújel miatti többletköltségek és a megszüntetés költségeinek összehasonlítása. Sínek Világa, No. 5, 2011, pp. 21-29, 2011.
[26] Fischer Sz: A vasúti zúzottkő ágyazat alá beépített georácsok vágánygeometriát stabilizáló hatásának vizsgálata. PhD thesis, Széchenyi István University Faculty of Engineering Sciences, 148 p, 2012.
[27] http://www.mavintezet.hu/vmmszk/JVO_ref_en.htm (downloaded: 28.05.2015)

[28] http://www.tensi.hu/userfiles/files/Angol%20oldal/Vonat/Railjet.pdf (downloaded: 28.05.2015)
[29] http://www.mobility.siemens.com/mobility/global/sitecollectiondocuments/en/rail-solutions/locomotives/reference-list-en.pdf (downloaded: 28.05.2015)
[30] http://www.stadlerrail.com/en/vehicles/flirt/ (downloaded: 28.05.2015)
[31] http://www.bombardier.com/en/transportation/products-services/mainline-solutions.html (downloaded: 28.05.2015)
[32] http://en.wikipedia.org/wiki/M%C3%81V_Class_V63 (downloaded: 28.05.2015)
[33] http://en.wikipedia.org/wiki/M%C3%81V_Class_V43 (downloaded: 28.05.2015)
[34] http://erojr.home.cern.ch/erojr/Content/models/m41/M41_his.htm (downloaded: 28.05.2015)
[35] http://en.wikipedia.org/wiki/M62_locomotive (downloaded: 28.05.2015)
[36] http://hu.wikipedia.org/wiki/Bzmot (downloaded: 28.05.2015)
[37] http://hu.wikipedia.org/wiki/M%C3%81V_6312_sorozat (downloaded: 28.05.2015)
[38] MÁV: Országos Közforgalmú Vasutak Pályatervezési Szabályzata. KÖZDOK, Budapest, 185 p, 1983.
[39] Gajári J: Vasútépítéstan I. Tankönyvkiadó, Budapest, 434 p, 1983.
[40] Széchenyi István Egyetem: Villamos vontatással üzemeltetett vasúti pályákon a sebességkorlátozások okozta többletköltségek csökkentési lehetőségeinek komplex vizsgálata. Research report, Győr, 97 p, 2012.
[41] Fischer Sz: Villamos vontatójárművek és motorvonatok vontatási energiafogyasztása, Sínek Világa, No. 1, pp. 13-18, 2013.

Acta
Technica
Jaurinensis

Vol. 8, No. 3, pp. 257–266, 2015
DOI: 10.14513/actatechjaur.v8.n3.381
Available online at acta.sze.hu

A New Metaheuristic Optimization Algorithm, the Weighted Attraction Method

G. Friedl[1], M. Kuczmann[2]

Széchenyi István University, Department of Automation
Egyetem 1, 9026, Győr, Hungary
E-mail: {friedl.gergely[1], kuczmann[2]}@sze.hu

Abstract: The paper presents a novel, particle behavior–based metaheuristic global optimization method. The idea behind the algorithm is based on attraction between particles, and in some aspects it is similar to the particle swarm optimization, but the interaction between particles is realized in a completely different way. The paper shows the main steps of the technique and some possible modifications. After that the comparison of efficiency and the speed of convergence with different well-known algorithms on two objective functions will be shown.

Keywords: *Weighted Attraction Method, metaheuristics, global optimization, swarm intelligence*

1. Introduction

Nowadays the metaheuristic algorithms are one of the most important tools for global optimization. These algorithms do not set almost any requirements to the objective functions, which have to be minimized. These methods can be applied to find the approximation of the optima for not continuous and not differentiable objective functions, even if they cannot be expressed in closed-form. The members of this algorithm family are usually inspired by nature, e.g. the genetic algorithm [1, 2] (GA), the bacterial evolutionary algorithm [3, 4] (BEA), and the particle swarm optimization [5–7] (PSO). These techniques deal with many disadvantages as well, e.g. the convergence speed of GA and BEA can be very slow or extremely decreasing, on the other hand, the PSO can *stuck* at local minimum. It is not exact which algorithm is better than the others, the efficiency is hardly depending on the objective function [8]. In some cases the calculation of the fitness function is very time consuming, the number of function evaluations has to be minimized to access fast runtime.

During our research the main goal was to develop an algorithm that is able to reach fast convergence with minimal number of function evaluations without being stuck. This qualities are very important for an optimization technique, because in a lot of cases the

fitness value can be calculated numerically, and the optimization process can take a huge amount of time. The main idea behind this newly proposed technique is the gravitational attraction between particles. In some aspects it is similar to the PSO, but the determination process of the next searching points are different. The following section introduces the main steps and the modification possibilities. After that, the third section shows the comparison of this method with some another techniques on two test objective function, the Ackley function and the Rosenbrock function.

2. The Weighted Attraction Method

2.1. Basic Concepts of Optimization

The general mathematical form of an optimization process [9] of a *constrained* optimization problem is formulated in the following way:

$$\begin{aligned} \underset{x}{\text{minimize}} \quad & f(\boldsymbol{x}), && \boldsymbol{x} = [x_1, x_2, \ldots, x_n]^\mathsf{T} \in \mathbb{R}^n, \\ \text{subject to} \quad & g_l(\boldsymbol{x}) \leq 0, && l = 1, 2, \ldots, r, \\ & h_l(\boldsymbol{x}) = 0, && l = 1, 2, \ldots, s. \end{aligned} \tag{1}$$

Here $f(\boldsymbol{x})$ is the *objective function*, which has to be minimized, the vector $\boldsymbol{x}$ contains the *design variables*, $g_j(\boldsymbol{x})$ is for the *inequality constraint functions*, and $h_j(\boldsymbol{x})$ denotes the *equality constraint functions*. The functions f, g, and h are scalar functions, more precisely: $\{f, g, h\} : \mathbb{R}^n \to \mathbb{R}$. If the feasible space for the minimum is the whole search space, the problem is called *unconstrained*. The solution vector that exactly satisfies (1) will be denoted as $\boldsymbol{x}^*$, where $\boldsymbol{x}^* = \arg\min_{\boldsymbol{x}} f(\boldsymbol{x})$.

The metaheuristic optimization begins with a set of points on the search space with parameters selected randomly. These points are usually called as *individuals* or *particles*. Let us denote the number of the particles by k. The set of all individuals are called *population* or *swarm*, denoted by $\mathbf{X}$, where $\mathbf{X} \in \mathbb{R}^{k \times n}$. Based on the concept of the applied method, these individuals are moved to another place, or (if the applied method is the GA) replaced by the so–called *offspring*. The goodness of each individual is defined by the *fitness function* as $\boldsymbol{F} = \mathscr{F}\{\mathbf{X}\}$, where $\mathscr{F}$ is the fitness operator, and $\boldsymbol{F} \in \mathbb{R}^k$ is a vector containing the fitness values for all particles. The definition of the fitness function is not straightforward, for a single problem it is possible to define many fitness function from a lot of aspects, but for the simplest cases the fitness function can be equal to the objective function. The interaction between the individuals is based on their fitness value. The better individuals are taken into account better by these methods. These methods often deal with random searching operation, and if the applied method is some of the evolutionary type methods, this is usually called as *mutation*, otherwise it is just called as random search.

2.2. The Proposed Method

The main goal was to develop a new algorithm that is capable of global optimization using less number of individuals without decreasing the runtime. The main idea behind the proposed method is the gravitational attraction between particles. The power of the attraction is a function of the fitness values. This power generates a global particle movement, and this global movement can be used as an efficient global searching technique. The main steps of this method are the following:

1. **Initialization:** Creating an initial, randomly placed particle dispersion on the whole search space;
2. **Calculation of attraction:** Calculating the fitness function, and based on the fitness values of each particle, assigning attraction factor to each one of them;
3. **Moving:** Choosing search direction for each particle based on their movement in the past, and the actual resultant attraction direction;
4. **Explosion:** Scattering the particles if they are too close to each other, and their fitness value is almost equal.

The 1^{st} step is evaluated only once at the beginning of the optimization procedure. The steps 2–4 are running iteratively until the best particle meets the predefined requirements, or the iteration number reaches its maximum. These steps are described in detail in the followings.

2.2.1. Initialization

The 1^{st} step of the weighted attraction method is creating uniformly placed initial searching particles. The easiest case, when the design variables are simply bounded, that is, $a_i \leq x_i \leq b_i$, $i = 1, \ldots, n$, $a_i, b_i \in \mathbb{R}$, and $\boldsymbol{x} \in \mathbf{X}$. Let us denote the j^{th} particle as $\boldsymbol{x}_j$. Now, the matrix $\mathbf{X}$ that represents the swarm of randomly chosen particles can be built up as

$$\mathbf{X} = [\boldsymbol{x}_1, \ldots, \boldsymbol{x}_j, \ldots, \boldsymbol{x}_k], \tag{2}$$

where

$$x_{j,\,i} = a_i + (b_i - a_i)r, \tag{3}$$

and $r \in [0, 1]$ is a random number. The initialization procedure is more difficult if the constraining of the search space is more specific, e.g. the feasible space is an n dimensional sphere or an abstract body. The search space can be limited with the definition of the constraint functions mentioned in (1).

2.2.2. Calculation of the attraction function

After the fitness values are calculated, an attraction factor should be given to each particles. This factor is defined by the *attraction function*. For the determination procedure this algorithm recommends the following steps:

- Sorting the particles according to their fitness value;
- Mapping the swarm to the domain $[0, 1]$ ($\boldsymbol{F} \rightarrow \boldsymbol{F'}$). The extreme values of this interval are assigned to the best and the worst particles, and the other particles got proportionally determined values;
- An attraction function w has to be determined. If this function is linear and its slope is unit, the attraction factors $w(\boldsymbol{F'})$ are equal to the assigned values. Otherwise, the attraction factors of the particles are the related values of the attraction function wF', as can be seen in Fig. 1;

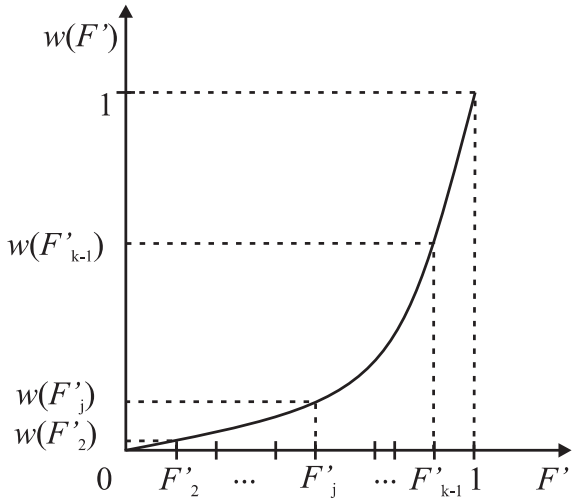

Figure 1. Explanation for the calculation of the attraction factors.

Because with the attraction function the factors of the attraction can be weighted, the algorithm will search more likely the better areas in the search space. The attraction function can be defined different ways. One of the ways can be seen in 1, where $w(0) = 0$ and $w(1) = 1$, and the function is monotonous. The other way is, when $w(0) < 0$. In this case the worst particles will repel the other particles from the bad parts of the objective function.

2.2.3. Moving

Based on the actual position of the particles and the corresponding attraction factors, the position of the *center of the mass* $\boldsymbol{c}$ in the m^{th} iteration can be defined as

$$\boldsymbol{c}^{(m)} = \frac{\sum_{j=1}^{k} \boldsymbol{x}_j^{(m)} w_j^{(m)}}{\sum_{j=1}^{k} w_j^{(m)}}. \tag{4}$$

The direction vectors pointing from the j^{th} particle to the center of mass can be easily calculated as

$$\boldsymbol{d}_j^{(m+1)} = \boldsymbol{c}^{(m)} - \boldsymbol{x}_j^{(m)}. \tag{5}$$

The new position of the j^{th} particle in the $(m+1)^{th}$ iteration is determined with the formula

$$\boldsymbol{x}_j^{(m+1)} = \boldsymbol{x}_j^{(m)} + \varphi_a \boldsymbol{d}_j^{(m+1)} + \varphi_b \boldsymbol{d}_j^{(m)}, \tag{6}$$

where φ_a and φ_b are random numbers. The initial searching directions $\boldsymbol{d}_j^{(0)}$ are optional, but mostly equal to zero. It can be useful if the algorithm takes into account the former searching directions in a better way. It can be easily realized (along with the update of the value $\boldsymbol{d}_j^{(m)}$) as

$$\boldsymbol{d}_j^{(m)} = \frac{u\boldsymbol{d}_j^{(m)} + v\boldsymbol{d}_j^{(m+1)}}{u+v}, \tag{7}$$

where u,$v \in \mathbb{R}^+$, and usually $v \geq u$.

In the early iterations this step usually provides fast convergence for the algorithm, but after awhile, if the particles are stuck in a local (or in fortunate cases global) minimum place, or the particles are in a *flat* area of the objective function, the convergence slows down, or even stops.

2.2.4. Explosion

The algorithm presented above can lead the global searching to stuck, because if every particle fall into the same local valley, the algorithm cannot jump out from here. It can be prevented by dispersing the particles, if a predefined *closeness* in position and fitness value has been reached. The authors recommends the dispersion process to be a normal distributed random dispersion that depends on the actual position and the extreme values of the design variables. A new value of the i^{th} design variable of the j^{th} particle can be calculated using the *Box–Muller–Marsaglia polar method* [10]. In algorithm 1, the value of α is predefined by the user. The greater value of α expands the expected radius of the dispersion.

The closeness condition is user–defined, but an optimal formula for it is unknown yet. It is clear that it depends on the variance of the fitness values and on the variance of the positions of the particles.

Algorithm 1 Box–Muller–Marsaglia polar method

procedure BMM(μ,σ) ▷ Normal random number generation.
  $\mu \leftarrow x_{j,\,i}$ ▷ Mean of the normal distribution is the actual value.
  $\sigma \leftarrow \alpha(\max(\mathbf{X}_{all,\,i}) - \min(\mathbf{X}_{all,\,i}))$ ▷ Formula for the variance.
  repeat
    $p, q \leftarrow [-1, 1]$ ▷ Uniformly distributed random number from the interval.
    $z \leftarrow p^2 + q^2$
  until $0 < z < 1$ ▷ Not to take the square root of a negative number.
  $x_{j,\,i_1} \leftarrow \mu + p\sigma\sqrt{-2\frac{\ln z}{z}}$
  $x_{j,\,i_2} \leftarrow \mu + q\sigma\sqrt{-2\frac{\ln z}{z}}$
  $r \leftarrow a \bmod b$
  return $x_{j,\,i_1}$ or $x_{j,\,i_2}$ ▷ Two random number generated, only one needed.
end procedure

3. Testing and comparison

This section is showing the comparison of the proposed algorithm with GA, BEA and PSO using the Ackley function and Rosenbrock function. The Ackley and Rosenbrock function are two well known test functions to evaluate properties of optimization methods.

The 2D Ackley function can be formulated as [12]:

$$f(x_1,x_2) = -20 \cdot \mathrm{e}^{-0.2\sqrt{0.5(x_1^2+x_2^2)}} - \mathrm{e}^{0.5(\cos(2\pi x_1)+\cos(2\pi x_2))} + 20 + \mathrm{e}. \tag{8}$$

This function is symmetric, has a numerous local minima, and a global minimum at the $x_1 = x_2 = 0$ point, where the function value is $f(0, 0) = 0$.
The most common form of the 2D Rosenbrock function can be formulated as [13]:

$$f(x_1,x_2) = (x_1 - 1)^2 + 100(x_2 - x_1^2)^2. \tag{9}$$

This function is asymmetric, has only one local (which is also a global) minimum, and the global minimum is at the $x_1 = x_2 = 1$ point, where the function value is $f(1, 1) = 0$.

On the objective functions, two different tests were made:

1. Optimization with 10 searching particles/individuals on the $-10 \leq x_1, x_2 \leq 10$ domain;
2. Optimization with 100 searching particles/individuals on the $-100 \leq x_1, x_2 \leq 100$ domain.

To test the robustness of the algorithm, every optimization process were made 100 times

and lasted 1000 period. In these cases the fitness functions were equal to the objective functions.

In Fig. 2 and 3, the comparison of the algorithms searching the minimum of the Ackley function is presented, in addition to the settings mentioned above.

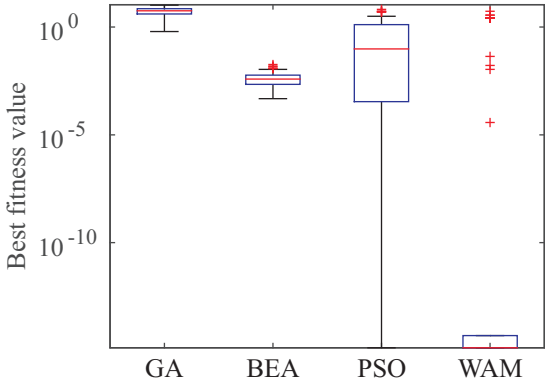

Figure 2. Optimization on the Ackley function, first case.

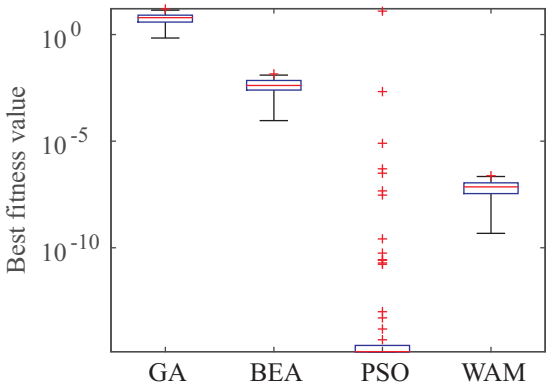

Figure 3. Optimization on the Ackley function, second case.

The presented figures were created by the `boxplot` function of `Matlab`. On each box the central mark is the median, the edges of the box are the 25^{th} and 75^{th} percentiles, the whiskers extend to the most extreme data points not considered outliers, and outliers are plotted individually [11]. In the first case, the WAM outperforms the other algorithms, in the worst processes it provided results at least as good as the other algorithms, bit in

the second case, with a lot of searching particles, the algorithm could not get any closer to the global minimum. The optimization processes were usually started with very fast convergence, but in the area of the minimum, the particles were jumping over the $[0, 0]$ point.

The comparisons of the algorithms on the Rosenbrock function in the two cases mentioned above can be seen in Fig. 4 and 5.

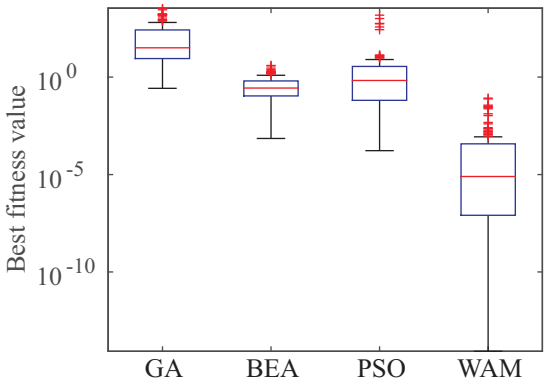

Figure 4. Optimization on the Rosenbrock function, first case.

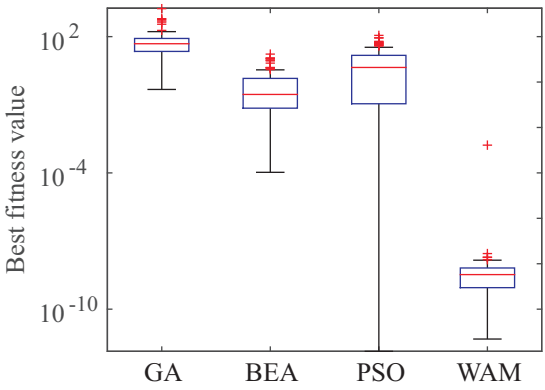

Figure 5. Optimization on the Rosenbrock function, second case.

Now in both cases, the WAM provided better solutions than the other applied algorithms, and in the second case, with more particle on greater domain the WAM could perform better approximation of the global minimum, and this contradicts the previous experiences.

The following figures show the typical trajectory of a particle during the optimization process. The empirical experiments showed that if the objective function is symmetrical like the Ackley function, the particles follow a spiral orbit during the searching process, but in the non-symmetrical case this behaviour was not experimented (see in Fig. 6).

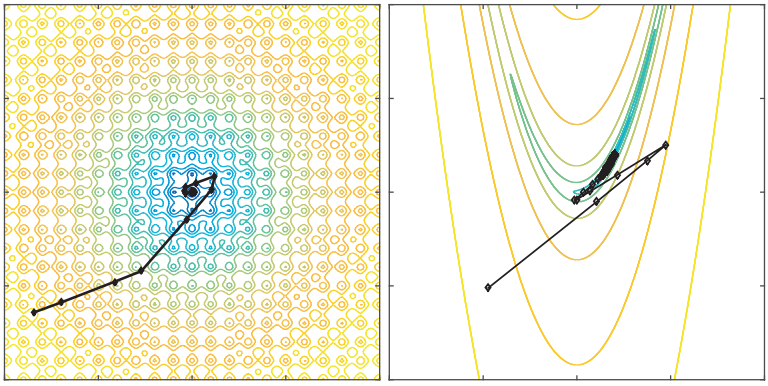

(a) Ackley function *(b) Rosenbrock function*

Figure 6. Typical trajectory of a searching particle.

4. Conclusions

The paper proposed a metaheuristic optimization tool named as Weighted Attraction Method. The main idea behind the algorithm was the gravitational attraction between particles. The concept is supplemented with a step that is responsible for the scattering of the particles preventing the algorithm being stuck. The comparison of the algorithm with other well known techniques were presented in Section 3. The Weighted Attraction Method were able to outperform the other techniques in the most cases, especially when the number of the searching particles were low. This property makes the algorithm even more effective, because it deals with fast convergence while the number of the fitness function evaluation remains low. The main disadvantage of the algorithm is that an exact optimal formula for the closeness of the particles does not exist yet. Now it seems that the best opportunity for this could be an adaptive *closeness condition* with adaptive dispersion scale.

The proposed algorithm will used to optimize antenna geometries, when the objective function is a strictly specified radiation pattern. The algorithm is believed to accelerate this optimization task, because it appears to be suitable for problems, where the evaluation of the fitness function is the most time consuming step.

References

[1] Holland JH.: Adaption in Natural and Artificial Systems, University of Michigan Press, Massachusetts, 1975

[2] Sumathi S, Hamsapriya T, Surekha P: Evolutionary Intelligence - An Introduction to Theory and Applications with Matlab, Springer, India, 2008

[3] Nawa NE, Hashiyama T, Furuhashi T, Uchikawa Y: Fuzzy Logic Controllers Generated by Pseudo-Bacterial Genetic Algorithm, In Proceedings of the IEEE International Conference on Neural Networks, vol. 4, pp. 2408—2413, Houston, 1997
DOI: 10.1109/ICNN.1997.614446

[4] Nawa NE, Furuhashi T: Fuzzy system parameters discovery by bacterial evolutionary algorithm, IEEE Transactions on Fuzzy Systems, vol. 7, no. 5, pp. 608-–616, 1999
DOI: 10.1109/91.797983

[5] Kennedy J, Eberhart R: Particle swarm optimization, In Proceedings of the IEEE International Conference on Neural Networks, vol. 4, pp. 1942-–1948, Perth, 1995
DOI: 10.1109/ICNN.1995.488968

[6] del Valle Y, Venayagamoorthy GK, Mohagheghi S, Hernandez J-C, Harley RG: Particle Swarm Optimization: Basic Concepts, Variants and Applications in Power Systems, IEEE Transactions on Evolutionary Computation, vol. 12, no. 2, pp. 171–195, 2008
DOI: 10.1109/TEVC.2007.896686

[7] Neri F, Mininno E, Iacca G: Compact Particle Swarm Optimization, Information Sciences, vol. 239, pp. 96–121, 2013
DOI: 10.1016/j.ins.2013.03.026

[8] Wolpert DH, Macready WG:No Free Lunch Theorems for Optimization, IIEEE Transactions on Evolutionary Computation, vol. 1, no. 1, pp. 67–82, 1997
DOI: 10.1109/4235.585893

[9] Snyman JA: Practical Mathematical Optimization, Springer, New York, 2005

[10] Luke S: Essentials of Metaheuristics, Lulu, second edition, 2013
available at http://cs.gmu.edu/∼sean/book/metaheuristics/

[11] Matlab, www.mathworks.com, (last visited: 06 May 2015)

[12] Ackley DH: A connectionist machine for genetic hillclimbing, Kluwer Academic Publishers, Boston, 1987

[13] Rosenbrock HH: An automatic method for finding the greatest or least value of a function, The Computer Journal, vol. 3, pp. 175–184, 1960
DOI: 10.1093/comjnl/3.3.175

Acta
Technica
Jaurinensis

Vol. 8, No. 3, pp. 267–279, 2015
DOI: 10.14513/actatechjaur.v8.n3.376
Available online at acta.sze.hu

A Wavelet Transform Based Study on the Representativeness of Preselected Frequency Points of the Insertion Loss Function in Fuzzy Performance Evaluation of Access Network Links

F. Lilik[1], Sz. Nagy[1], L. T. Kóczy[2]

[1]**Széchenyi István University, Department of Telecommunications**
Egyetem tér 1, 9026, Győr, Hungary
E-mail: lilikf@sze.hu

[2]**Széchenyi István University, Department of Information Technology**
Egyetem tér 1, 9026, Győr, Hungary

Abstract: The performance evaluation of telecommunication networks and connections is a usual problem of telecommunications service providers and network owners. The performance evaluation in our previous approach is strongly (but not exclusively) based on the insertion loss values of the wire pairs measured at certain discrete frequency points. According to experimental results, the usage of these frequencies leads to correct evaluation, however, the theoretic verification of the correctness of the placement of these points seems to be necessary. The study was carried out using wavelet analysis, comparing the insertion loss values measured at the discrete frequency points with the wavelet transformed sections of the insertion loss functions corresponding to them. In this paper, using wavelet transform, we have studied whether the previously selected characteristic frequencies represent well the frequency domain around them also rules using wavelet transformed data are compared to the rules of the method based on characteristic frequencies.

Keywords: *telecommunications, performance evaluation, access networks, fuzzy inference, wavelet analysis*

1. Introduction

The examination of the correctness of the antecedent dimension selection for a telecommunications performance evaluation approach based on fuzzy models is presented in this paper. This new approach is appropriate for the classification of the telecommunications access networks' individual wire pairs for SHDSL (Symmetrical High Speed Digital Subscriber Line) [1] connections according to the possibly available data transfer rate (bit

rate), however it can be generalized for any type of digital access network links. SHDSL is a symmetrical member of the DSL telecommunications transmission family which was evolved definitely for the copper wire pairs of the access networks. (According to recent studies, e.g., [2], copper wire pairs of access networks will be used for the installation of new telecommunication connections even beyond 2040, however, the replacement of the traditional metallic transmission medium by fibre optical ones has been recently announced in Hungary.)

Similarly to some other performance evaluation techniques in the field of telecommunications, our method uses observed electrical properties of the measured lines.[3] Differently from the currently used methods, our qualification is made according to mostly the measured values of insertion loss by fuzzy rule bases in our approach. [4]

In Fig. 1. insertion loss characteristics of the lines studied in this contribution can be seen. In accordance with the practice of telecommunication service providers, different ranges of bit rates were separated into different clusters. Typical examples of this classification can be seen in Fig. 2. Values of bit rates ascend from cluster 1 to cluster 5.

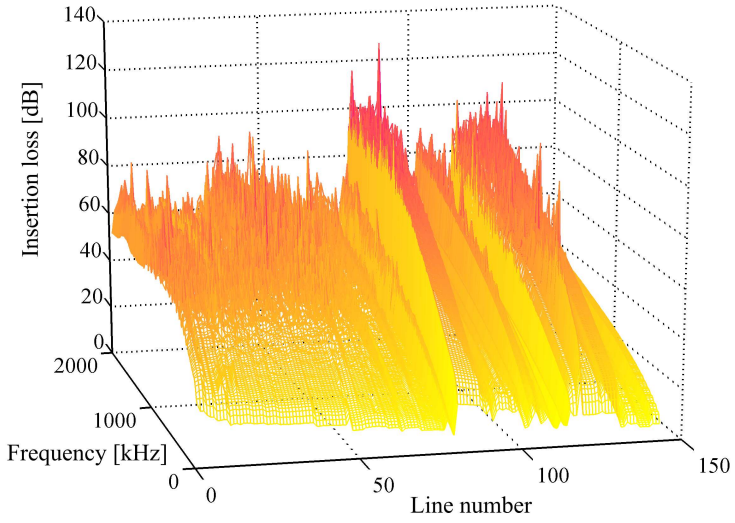

Fig. 1. Insertion loss characteristics of the observed lines.

Fig. 2. shows that the ranges defined by different bit rate clusters are overlapping, which makes the problem of wire pairs' performance evaluation nondescript and hardly classifiable by traditional methods. For such problems the fuzzy set theory was suggested by L. A. Zadeh in 1965 [5] and a widely used, successful application was introduced by E.

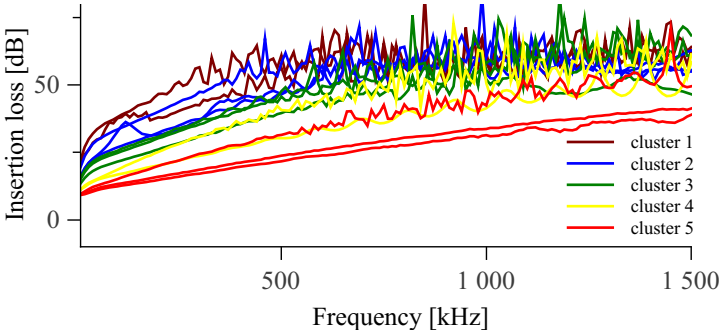

Fig. 2. Examples of the classification of insertion loss characteristics by bit rate clusters.

H. Mamdani [6] in 1975. In our approach Mamdani's fuzzy inference method has been applied.

Our approach is predominantly based on the insertion loss of the lines. Even though insertion loss values were measured only in 200 discrete points of the frequency in this study, this physical property of the wire pairs is continuous. In order to avoid the difficulty of handling continuous functions or too many values in the antecedent part of the evaluation, some of the frequencies were selected for the actual decision-making. Based on experimental results, these frequencies are 100 kHz, 500 kHz, 750 kHz, 1000 kHz, 1250 kHz and 1500 kHz. The distance between the characteristic frequencies is uniformly 250 kHz, the only difference is at 100 kHz. This irregularity of the position of the characteristic frequencies is explained by the stronger separation of the insertion loss functions around 100 kHz.

Measured insertion loss values at the 6 characteristic frequencies (see in Fig. 3.) were used in the construction of fuzzy rule bases. Based on these data, two types of rule bases were created, one type was made directly from the measured values (later referred to as D-type), and another by evolutionary algorithm [7] (E-type), where measured values were used as teaching samples. The D-type rule base has five rules – according to the five bit rate clusters – and six antecedent dimensions (the insertion loss values at the characteristic frequencies), and its fuzzy sets are triangular. One of the rules of the D-type rule base can be seen in Fig. 4 graphically, as an example.

The E-type rule base is not in direct connection with the five output clusters. It has 10 rules, however, also it has six antecedent dimensions. In this case the fuzzy sets are trapezoidal. See Fig. 5.

Both type of rule bases has been tested by evaluating previously unknown wire pairs. Comparing to the results of other, widely available and used pre-qualification methods, the

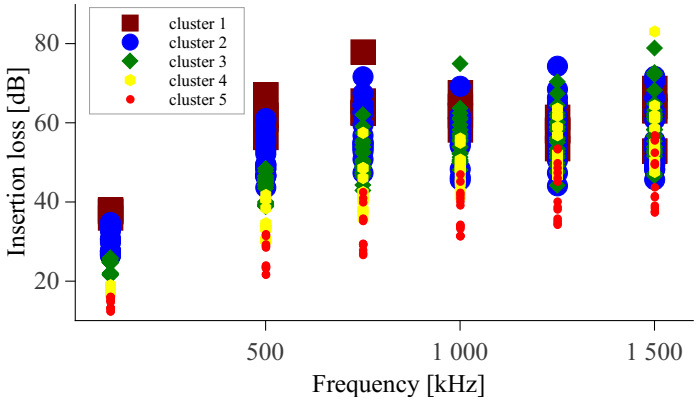

Fig. 3. Measured insertion loss values of the lines used for rule base construction at the characteristic frequencies.

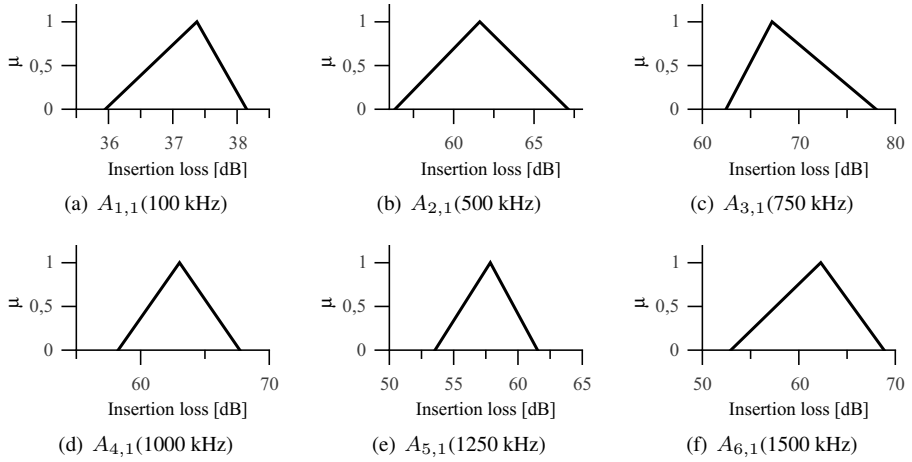

Fig. 4. Triangular antecedent sets of the 1^{st} rule from the D-type rule base. The left axis shows the membership values and the bottom axis shows the insertion loss. The closures of the supports fo the membership functions were defined by the limits of the measured insertion loss values, whereas the core points were the mean values of the measured data. (In fuzzy set theory we study not only weather an element belongs to a set or not, but also how much it belongs to the set. The rate of this "belonging" is called membership value of the given element.)

success rate of our approach reached the success rate of the most accurate methods, and

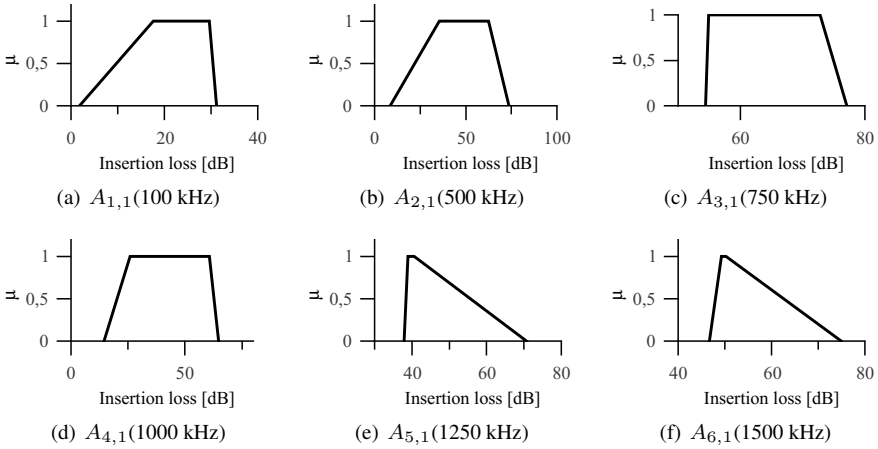

Fig. 5. Trapezoidal antecedent sets of the 1^{st} rule from the E-type rule base. The left axis shows the membership values and the bottom axis shows the insertion loss.The measured data were grouped according to their performances and were used as teaching samples in the construction of the rule bas by the evolutionary algorithm defined in [7].

using different rule bases constructed from insertion loss values measured in areas with different line noise, the success rate was higher than in case of other methods [8].

Correctness of the frequency points used in rule bases is confirmed by the results of the tests, however, this verification is based on experiments carried out on finite number of wire pairs. Possibly there can be – and according to our expectations there are – wire pairs which have severe deviations in insertion loss exactly at the characteristic frequencies that provide the basis of our qualification method. In such cases the evaluation will be failed, the lines will be classified not into the correct, but its neighbouring cluster. The reason for this problem is that the insertion loss is studied not in the whole frequency range but only at discrete points of the frequency, therefore it seems to be important to examine how representative the insertion loss values at the selected frequency points are to the ranges around them. In this paper we apply wavelet analysis to determine, whether the large-scale behaviour of the insertion loss function can be represented well by the selected characteristic frequencies.

Wavelet theory – summarized e.g., in [9–11] – became one of the basic data procession methods in the past three decades. Even though the most successful branch of their application is the image compression – wavelets are used from fingerprint databases [12] to Mars rovers [13] and the JPEG2000 compressor [14] – one of the reasons wavelets arose was the analysis of one dimensional data, namely seismic echoes in oil research [15]. In the following considerations we also use wavelets for one dimensional data analysis: we

gain information about the structure of the insertion loss-frequency function by wavelet analysis.

2. On wavelet analysis

Fourier analysis [18] of a signal can give information about the structure of the signal: it can tell the amount of slowly varying – low frequency – and rapidly varying – high frequency – components. The main problem with Fourier analysis from the practical applications point of view was that it requires infinite signal. In order to be able to gain information about the slowly and rapidly varying components of a real measured signal a short time Fourier transform or windowed Fourier transform was introduced. The basic idea behind the windowed fourier transform

$$\mathcal{F}_b\{f\}(\omega) = \int_{-\infty}^{\infty} w(t-b)\, f(t)\, e^{-i\omega t}\mathrm{d}t. \tag{1}$$

is to make a short snapshot of the studied function $f(t)$ with a short window function $w(t)$ at any point b and transform the thus arisen function. Of course, the integral of the resulting functions $\mathcal{F}_b\{f\}(\omega)$ along the variable b, we get the usual Fourier transform of the function,

$$\int_{-\infty}^{\infty} \mathcal{F}_b\{f\}(\omega)db = \mathcal{F}\{f\}(\omega).$$

The selection of the window function is a key for an effective transform. Dennis Gábor [17] suggested to use Gaussian type window

$$w_\alpha(t) = \frac{1}{2\sqrt{\pi\alpha}}\, e^{-\frac{t^2}{4\alpha}}$$

and the windowed Fourier transform with such window functions are still called Gabor transform.

However, if we look at (1) from another point of view, it can be seen as a transform with the windowed sinusoidal function

$$W_{b,\omega}(t) = e^{i\omega t}\, g(t-b),$$

thus

$$\mathcal{F}_b\{f\}(\omega) = \int_{-\infty}^{\infty} (W_{b,\omega}(t))^*\, f(t)\mathrm{d}t, \tag{2}$$

with * meaning complex conjugation. The shape of the window function $W_{b,\omega}(t)$ for the Gabor transform is given in Fig. 6 with $b = 0$ and three values of ω.

The wavelet transform of a signal has the same approach as formula (2), only the window function has a different construction,

$$\psi_{b,a}(t) = |a|^{-1/2}\, \psi\left(\frac{t-b}{a}\right),$$

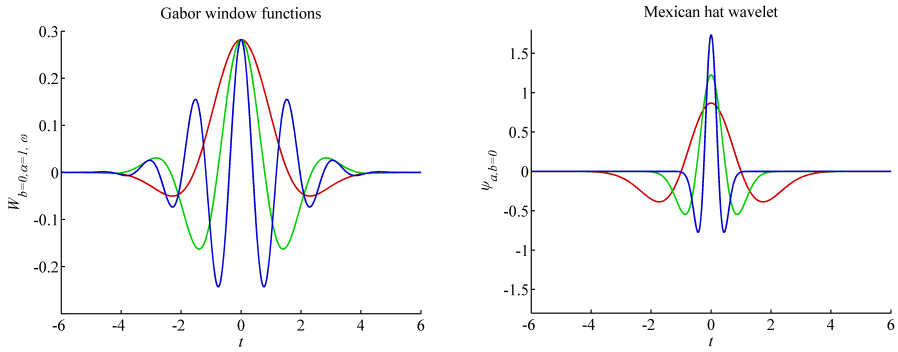

Fig. 6. The window function $W_{0,\omega}$ of the Gabor transform (left) with $\alpha = 1$, and the Mexican hat wavelet $\psi_{a,0}$ (right). Both function types are given for three resolutions, i.e., $\omega = 1$ (red), $\omega = 2$ (green), $\omega = 4$ (blue) for the Gabor transform function and $a = 1$ (red) $a = 2$ (green), $a = 4$ (blue) for the wavelet. All functions are centered to 0, i.e., the shift index $b = 0$. Arbitrary units.

resulting in the transform

$$\mathcal{W}_\psi\{f\}(b,a) = |a|^{-1/2} \int_{-\infty}^{\infty} \psi^*_{b,a}(t) f(t) \mathrm{d}t.$$

The wavelet function $\psi_{b,a}(t)$ is generated from the mother wavelet by simple shifting and shrinking/stretching, thus the window functions have the same shape for the fine scale and large-scale behaviours, only their widths varies, as it can be seen in Fig. 6. This shape is usually consisting of some waves in a short interval, hence the name little waves, or wavelets.

Generating the wavelet has lots of freedom, the only constraint that has to be fulfilled is

$$\int_{-\infty}^{\infty} \frac{1}{\omega} \left|\mathcal{F}\{\psi\}(\omega)\right|^2 d\omega < \infty.$$

The application of the wavelets is similar to that of the Fourier transform, besides data/signal analysis, they can be used for solving differential equations [19–21].

For our purposes the discrete version of the wavelet transform is more suitable as we have a series of insertion loss values measured at discrete frequencies. The realization of a discrete wavelet transform is relatively simple: one step consists of a filtering and a downsampling as it can be seen in Fig. 7. This step can be applied constitutively, as long as the number of the steps do not exceed the 2-based logarithm of the number of the points to be analysed. Both the high pass and the low pass convolution filter have the

same coefficients during the transformation process, and means approximately halving the resolution (frequency) at each step.

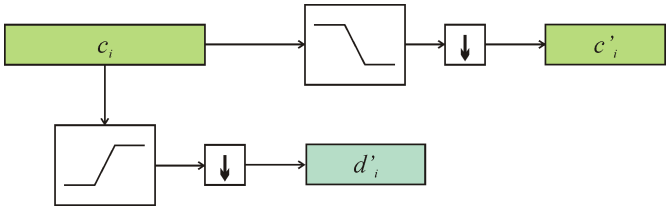

Fig. 7. One step of the discrete wavelet transform. After the high pass (direction down) and low pass (direction right) convolutional filters a downsampling by two unit is plotted by the downward arrow. The transformed vectors c'_i and d'_i are approximately half in the size compared to the original c_i.

The results will be the lowest resolution level (last) vector c'_i and all the vectors d'_i. The vectors d'_i carry the information about the fine-scale behaviour, whereas the vectors c'_i is a kind of weighted average, i.e., it describes the larger scale behaviour. Of course, the expressions "fine scale" and "large-scale" are roughening as the transformation steps carry on.

Theoretically the total number of the elements of the resulting vectors is approximately the same as that of the original vector c_i, so no information is lost in the process. In case of data compression, many of the vector components d'_i are omitted, as they are close to zero in the smooth parts of the functions, images, distributions that represented by the original c_i.

There exists a backward transform, which is the opposite of the one given in Fig. 7, from vectors d'_i and c'_i after an upsampling – filling in zeros between each of the vector elements – the inverse of the convolutional filters is applied and the results of the two branches are summarized. However, this step is not important for our purposes.

In the following considerations we do not study the fine scale components resulting from the analysis of the measured insertion loss data, only the rough scale coefficients. To be more precise, we are studying environments of the selected frequencies by two different wavelet families: Haar and the second Daubechies wavelet transform. As the Haar functions have only 2 filter coefficients (both 1), and due to the downsapmling there are no overlaps between the originals c_i of the neighbouring transformed points c'_i and d'_i, their low-pass components mean only an averaging. The low-pass transform with the 4-coefficient Daubechies filters means overlapped averaging with non-uniform coefficients. Both results gives information about the large-scale behaviour around the selected points, thus the representativeness of the frequency points to their environment.

3. Representativeness of the selected frequencies

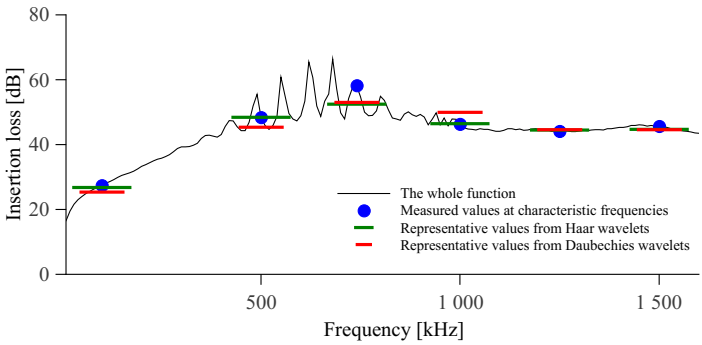

Fig. 8. Measured insertion loss and calculated levels by wavelet transformation.

One random wire pair's measured insertion loss function and its representative values resulting from the function's wavelet transforms can be seen in Fig. 8. Even though the insertion loss values measured at the six selected frequency points (indicated by blue ellipses) are close to the levels calculated by wavelet transformation (indicated by olive green lines) in the figure, in the case of a single line, the measured values at the characteristic frequencies have differences from the wavelet transformed values.

To check the deviations in case of all measured wire pairs, the wavelet transformed values versus the measured ones are plotted in Fig. 9. It can be seen that the dots are located very close to the ideal $45°$ line in case of higher insertion loss and higher frequencies, and follow the line in case of lower ones. It means, that although in case of some wire pairs the measured values and the levels calculated by wavelet transformation differ from each other – though this deviation is not too high –, statistically, the ranges of the insertion loss function are characterized well by the measured values at the six selected respective frequencies.

Though the whole insertion loss function is decently characterized by the values measured at the selected frequencies also in case of individual wire pairs, the alignment of the measured values with the ranges defined by the insertion loss values of the lines belonging to the corresponding bit rate clusters are much more important. The reason is that the antecedent fuzzy sets of the rule bases used in the performance evaluation represents a sort of model of the ranges disposed by the insertion loss values measured at the given frequency points. The selected discrete frequency points are appropriate if the wire pairs' physical properties measured at them fit to the ranges created from the insertion loss functions' wavelet transformed levels. Fig. 10 shows the results of this comparison. Corresponding areas derived from the wavelet transformed sections of the functions, denoted by red and blue lines, are followed by the ranges of measured values denoted by black lines in case of

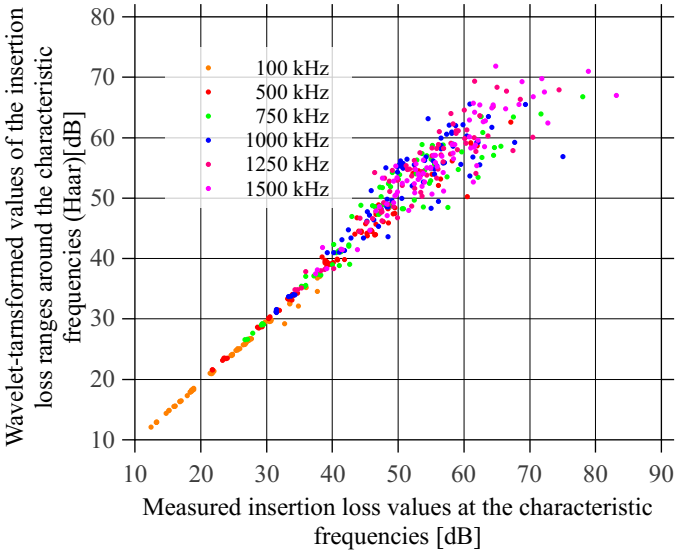

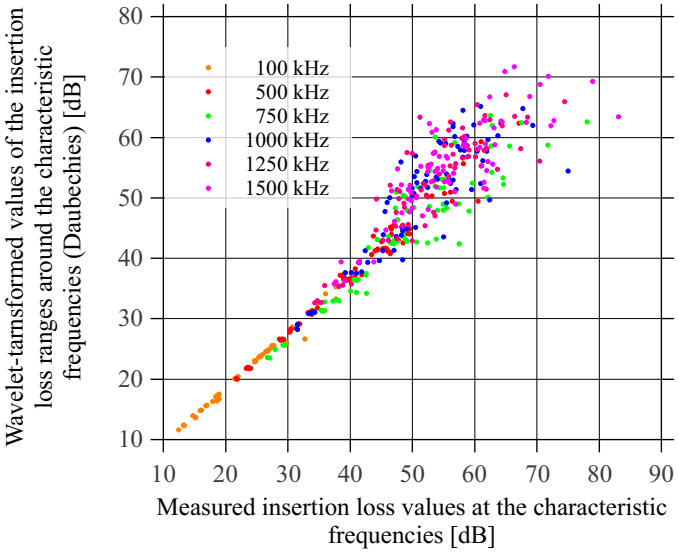

Fig. 9. Measured insertion loss and calculated levels by two different wavelet transformations of the lines used for deriving our rule bases. It can be seen that the selected frequency points of the measured functions represent quite well the large scale behaviour, however, the Haar wavelet transformed values lay significantly closer to the values measured than those of Daubechies transformed ones.

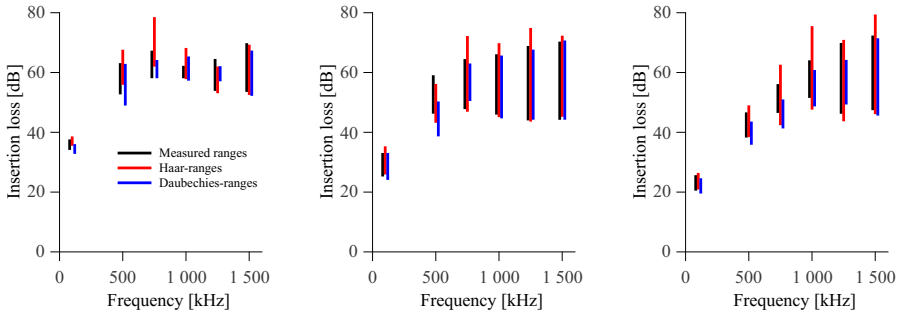

(a) Cluster 1 (b) Cluster 2 (c) Cluster 3

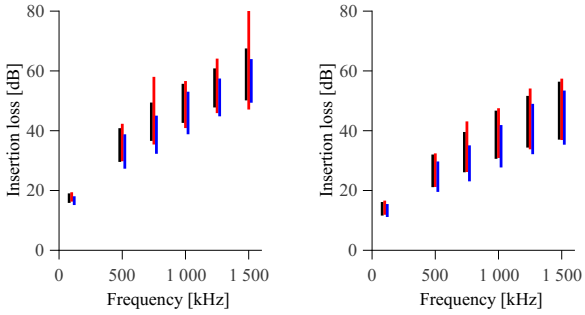

(d) Cluster 4 (e) Cluster 5

Fig. 10. Comparison of the insertion loss ranges measured at the characteristic frequencies with the ranges of wavelet transformed function environment around the characteristic frequencies by bit rate clusters.

all bit rate clusters. Minor deviations of the wavelet transformed ranges from the measured values can be noticed only in case of the cluster belonging to the lowest bit rates. As clear and strict mathematical formula does not exist for the connection between the physical properties of the wire pairs and the available maximal bit rates this kind of small deviation is acceptable in performance evaluation. The importance of the discrepancy is lessened by the fact that the deviations of all examined wire pars are depicted together in the same figure, but in the case of singular lines, generally, this degree of the deviation can be noticed only at one frequency point.

4. Conclusions, future work

The examination of characteristic frequencies of insertion loss in performance evaluation of access networks' wire pairs was presented. After the description of a novel approach for the performance evaluation and the problem with the used frequency points in the

evaluation, the usage of the wavelet transformation as method of the examination was explained. Beside experimental observations, also theoretical results showed that the selected frequency points are appropriate for being used as characteristic frequencies in the measurement of the wire pair evaluation.

Using ranges of wavelet transformed sections of the functions of physical properties which are the basis of the evaluation showed that new type, wavelet based rule bases can help to reduce the number of the antecedent dimensions. In the future the reduction of the antecedent dimensions' number by wavelet analysis is planned.

Acknowledgement

The publishing of this paper was supported by the Hungarian National Research Fund (grant no. K105529 and K108405).

References

[1] ITU-T: Recommendation G. 991.2, Single-pair high-speed digital subscriber line (SHDSL) transceivers, 02/2001

[2] Ödling P et al.: The Fourth Generation Broadband Concept, Communications Magazine, IEEE, vol. 47 issue 1, pp. 62-69,January 2009
DOI: 10.1109/MCOM.2009.4752678

[3] Goralski W: xDSL Loop Qualification and Testing, Communications Magazine, IEEE, vol. 37 issue 5, pp. 79-83, May 1999,
DOI: 10.1109/35.762860

[4] Lilik F, Kóczy LT: The Determination of the Bitrate on Twisted Pairs by Mamdani Inference Method, Issues and Challenges of Intelligent System and Computational Intelligence, Studies in Computational Intelligence, vol 530, pp.59-74, Springer International Publishing, 2014
DOI: 10.1007/978-3-319-03206-1_5

[5] Zadeh LA: Fuzzy sets, Inf. Control, Vol. 8., pp:338-353, 1965

[6] Mamdani EH, Assilian S: An Expriment in Linguistic Synthesis with a Fuzzy Logic Controller, International Journal of Man-Machine Studies, Vol. 7, pp. 1-13, 1975

[7] Balázs K, Kóczy LT: Constructing Dense, Sparse and Hierarchical Fuzzy Systems by Applying Evolutionary Optimization Techniques, Applied and Computational Mathematics, Vol. 11, No. 1, pp. 81-101, 2012

[8] Lilik F, Kóczy LT: Performance Evaluation of Wire Pairs in Telecommunication Networks by fuzzy and Evolutionary Models, IEEE Africon 2013 Conference Mauritius,

9th-12th September 2013, pp. 712-716,
DOI: 10.1109/AFRCON.2013.6757602

[9] Daubechies I: Ten Lectures on Wavelets, CBMS-NSF regional conference series in applied mathematics 61, SIAM, Philadelphia, 1992

[10] Chui CK: An Introduction to Wavelets, Academic Press, San Diego, 1992

[11] Goedecker S: Wavelets and their application for the solution of partial differential equations in physics, Cahiers de physique, 4. Presses polytechniques et universitaires romandes, Lausanne, 1998

[12] Montoya Zegarra JA, Leiteb NJ, da Silva Torres R: Wavelet-based fingerprint image retrieval, J. Comput. Appl. Math., Vol. 227, pp. 297-307, 2008
DOI:10.1016/j.cam.2008.03.017

[13] Kiely A, Klimesh M: The ICER Progressive Wavelet Image Compressor, IPN Progress Report 42-155, November 15, 2003

[14] Christopoulos Ch, Skodras A, Ebrahimi T: The JPEG2000 Still Image Coding System: An Overview, IEEE Trans. Consumer Electronics, Vol. 46, pp. 1103-1127, 2000
DOI:10.1109/30.920468

[15] Grossmann A, Morlet J: Decomposition of hardy functions into square integrable wavelets of constant shape, SIAM J. Math. Anal., Vol. 15, pp. 723-736, 1984

[16] Haar A: Zur theorie der orthogonalen funktionen systeme, Math. Ann., Vol. 69, pp. 331-371, 1910

[17] Gabor D: Theory of communication, J. IEEE, Vol. 93, pp. 429-457, 1946

[18] Fourie M: Theorie Analitique de la Chaleur, Chez Firmin Didot, Paris, 1822

[19] Urban K: Wavelet Methods for Elliptic Partial Differential Equations, Oxford University Press, Oxford, 2009

[20] Dahmen W: Wavelets and Multiscale Methods for Operator Equations Acta Numerica Vol. 6, p. 55, 1997

[21] Pipek J, Nagy Sz: An Economic Prediction of Refinement Coefficients in Wavelet-Based Adaptive Methods for Electron Structure Calculations J. Comput. Chem., Vol. 34, p. 460-465, 2013
DOI:10.1002/jcc.23154